Journal Pre-proof

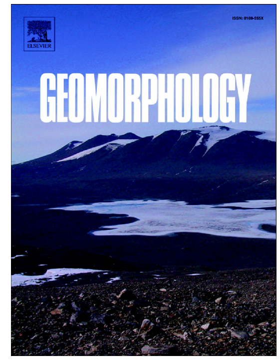


# Debris flow–derived sediment routing and storage in a mountain river network: a D-CASCADE application in the Trebbia-Aveto River (Italy)

Cristobal A. Padilla M., Francesco Lelli, Alessandro Corsini

PII: S0169-555X(26)00380-6

DOI: https://doi.org/10.1016/j.geomorph.2026.110537

Reference: GEOMOR 110537

To appear in: *Geomorphology*

Received date: 3 February 2026

Revised date: 21 August 2026

Accepted date: 7 September 2026

# Title: Debris flow–derived sediment routing and storage in a mountain river network: a D-CASCADE application in the Trebbia-Aveto River (Italy)

**Authors: Cristobal A. Padilla M.[a,*], Francesco Lelli[a], Alessandro Corsini[a]**

**Affiliation: a) University of Modena and Reggio Emilia, Department of Chemical and Geological Sciences, Via Giuseppe Campi 103, 41125 Modena, Italy**

**(*) Corresponding Author Email address: cristobalpadilla@gmail.com**

## 1 Introduction

Landslides play a key role in the sediment budgets of mountain basins because they can produce and mobilize large volumes of sediment over short timescales (e.g. Schuerch et al., 2006; Korup et al., 2010;; Uchida et al., 2018). Hillslope failures are often the dominant control on catchment sediment yield and landscape evolution, exceeding the influence of channel erosion (Schlunegger et al., 2009; Bennett et al., 2013). Among landslide processes, debris flows typically have broad impacts along streams because their high mobility enables sediment to travel long distances, often reaching higher-order channels and propagating effects far downstream (Jakob and Hungr, 2005). Once sediment enters the basin's main channel, its routing and residence times depend on network-scale morpho-fluvial characteristics and on the structural and functional (dis)connectivity of the river system (Heckmann and Schwanghart, 2013; Bracken et al., 2015). Quantifying debris-flow sediment remobilization, i.e., the resulting downstream storage and export at basin scale, remains challenging because it requires spatially explicit, long-duration monitoring of sediment sources, transfers, and sinks (Hovius et al., 1997), even at the catchment scale (Schuerch et al., 2006; Schlunegger et al., 2009;).

Despite this complexity, recent advances in network-scale sediment connectivity modeling offer a tractable framework for reconstructing debris flow–derived sediment at the basin scale. Such model-based approaches provide a reproducible and comparatively low-cost alternative to intensive field monitoring while retaining the capacity to represent the key processes governing sediment supply, routing, and storage across entire river networks.

The objective of this work is to quantify how debris flow–derived sediments — hereafter referred to as the debris-flow sediment pulse (DFSP) — propagate through a basin-scale river network over a period of nearly a decade, by applying D-CASCADE, a dynamic, network-scale sediment (dis)connectivity model (Tangi et al., 2022). Although D-CASCADE is relatively recent, published applications demonstrate its utility (Tangi et al., 2023), and ongoing case studies are expanding its scope (Doolaeghe et al., 2025); its application to episodic, debris flow–derived sediment represents a novel context for the model. D-CASCADE builds on the CASCADE framework (Tangi et al., 2019), which has a proven track record for network-scale sediment routing and connectivity analysis and is supported by open-source toolboxes and case-study resources (Bizzi et al., 2021; Brierley et al., 2022). The model combines graph-based routing with empirical transport equations to reconstruct and forecast spatiotemporal patterns of sediment supply, delivery, and storage across entire basins.

## 2 Study area and debris flow events of 2015

### *2.1 Study area overview*

The study area is a sub-basin of the Trebbia River located in the Emilia–Romagna and Liguria regions of the northern Apennines, Italy (Figure 1). The sub-basin is delineated by an outlet situated upstream of the town of Bobbio and has been truncated to include almost exclusively the portion within the Emilia–Romagna Region, covering approximately 653.3 km². The elevation ranges from 260 m a.s.l. at the outlet at Bobbio to 1700 m a.s.l. approximately.

Bedrock in the basin is dominated by weak, highly fractured sedimentary units belonging to the Ligurian and Sub-Ligurian Units, deposited in the Piedmont–Ligurian Ocean from the Middle Jurassic to the Paleogene (Conti et al., 2020).

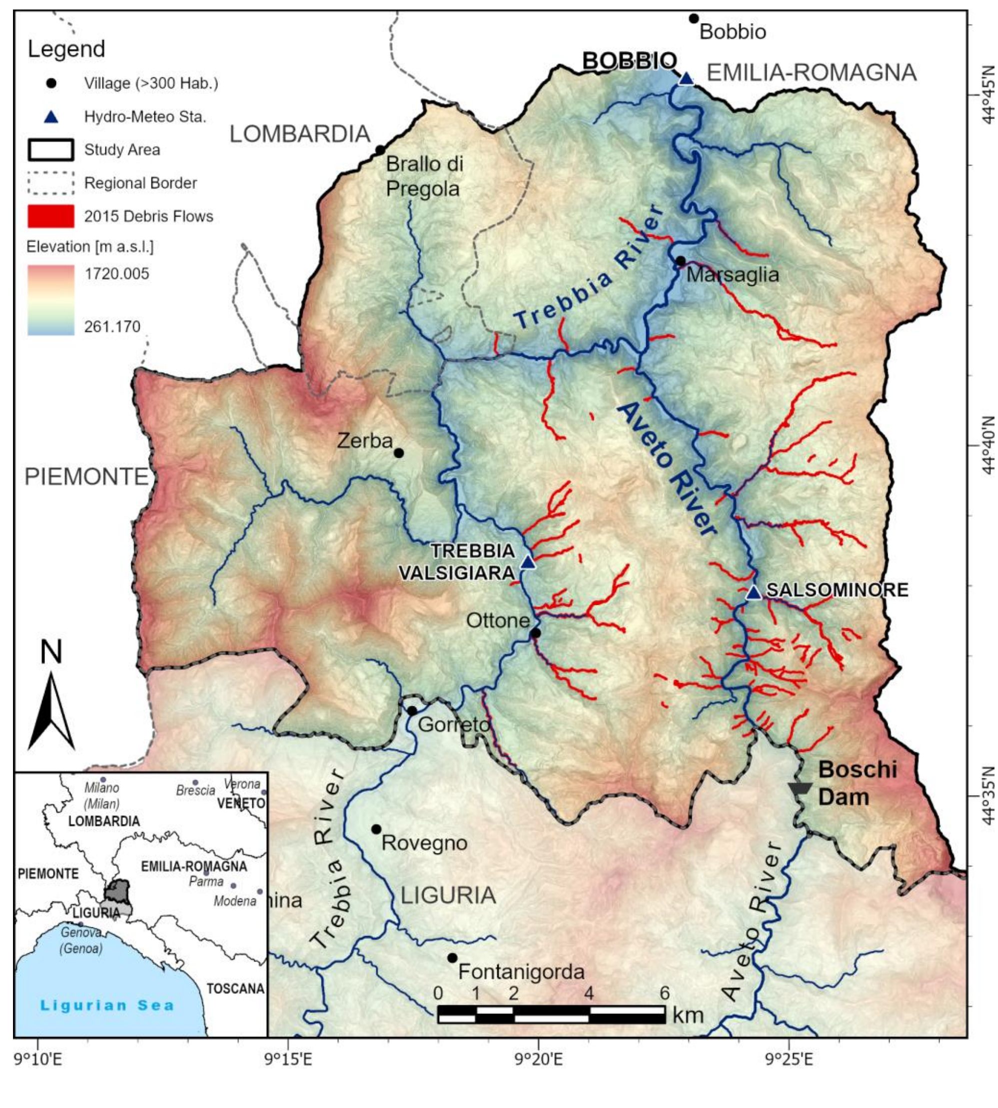


*Figure 1. Section of the Trebbia River basin defined as the study area (colored DEM). The upstream of the study area, part of the Trebbia river basin, but not included in this work, is represented in pale colors.*

### *2.2 Hydrometeorology*

The climate is characterized by a cold winter and a dry summer, with most of the precipitation occurring during autumn and spring, with October and April being the rainiest months (Bollati et al., 2014). The valley around Bobbio records an average annual precipitation of ~1,160 mm, with monthly maxima in late autumn (November ~140 mm $month^{-1}$). In the Aveto headwaters at Santo Stefano d'Aveto (near Boschi dam), annual precipitation increases to ~1,470–1,530 mm, with autumn maxima (October–November ~190–200 mm $month^{-1}$). Large mesoscale convective systems frequently develop in late summer and early autumn, producing severe rainstorms; individual episodes can deliver a substantial fraction of the annual total within hours (Ciccarese et al. 2021).

Based on daily average records from 2005 to 2024, the average discharge of the Trebbia River is 17.3 $m^3 s^{-1}$ at Bobbio station, with a maximum recorded of 574 $m^3 s^{-1}$ in 2009 and a minimum of 0.02 $m^3 s^{-1}$ in 2022. The months with the highest average daily discharges are November and December, with 31.2 $m^3 s^{-1}$and 28.3 $m^3 s^{-1}$, respectively. In the same period, the Trebbia Valsigiara and Salsominore stations recorded and average discharges of 6.42 $m^3 s^{-1}$ and 4.62 $m^3 s^{-1}$, respectively (Figure 2).

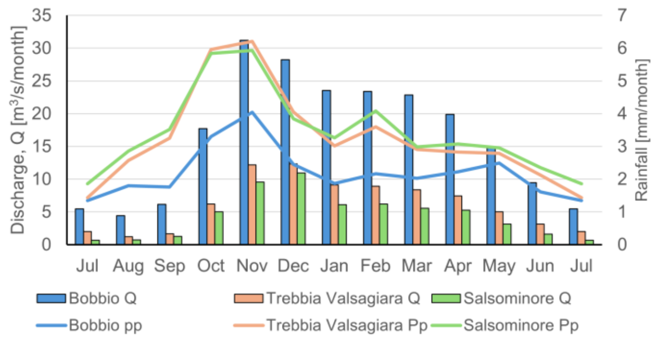


*Figure 2. Average daily discharge/rainfall per month in the Trebbia–Aveto river system, based on records from 2005 to 2024.*

## *2.3 Fluviomorphology*

The Trebbia River has a total length of 120 km, whereas the study reach encompasses 45.3 km. The area also includes one major tributary, the Aveto River, with 19.3 km within the study area boundaries.

Within the study area, the Trebbia–Aveto river system (TAR) displays a predominantly mountainous, confined single-thread morphology, with highly incised bedrock reaches that locally exhibit irregular sinuous segments in the upper catchment, transitioning downstream into partly confined sections (Rinaldi et al., 2012; Rinaldi et al., 2013; Bollati et al., 2014).

Consistent with the Montgomery and Buffington (1997) framework, the main channel of TAR include pool–riffle morphology in alluvial single-thread sections (bars, pools, and riffles formed over undulating gravel beds), and plane-bed morphology where confinement by valley walls suppresses bar development and pool spacing. Steeper and smaller tributaries commonly express cascade and step-pool morphologies, grading into colluvial/bedrock reaches where coarse particles and shallow flow depths constrain sediment mobility except during large floods.

The Trebbia River exhibits a well-defined longitudinal profile throughout the analyzed segment (Figure 3), characterized by the absence of major knickpoints. However, a distinct shift in the channel slope occurs at the confluence with the Aveto River. Upstream of this confluence (Upper Trebbia), channel slopes consistently exceed 0.6%, whereas downstream (Lower Trebbia), slopes fall markedly below this threshold, averaging approximately 0.5%. By contrast, the Aveto River shows a prominent knickpoint near the upstream entrance to the study area associated with the Boschi Dam (hydropower reservoir built in the 1920s), after which the channel flows through a short, steep, entrenched reach (≈ several kilometers, until a few hundred meter upstream Salsominore station) before re-establishing a broader, alluvial corridor toward its confluence with the Trebbia. In this post-dam segment of the Aveto, the predominance of bedrock and discontinuous alluvium indicates high transport capacity relative to sediment supply, consistent with mountain-river reach classifications where steep, confined channels tend toward supply-limited conditions and limited bar/pool development.

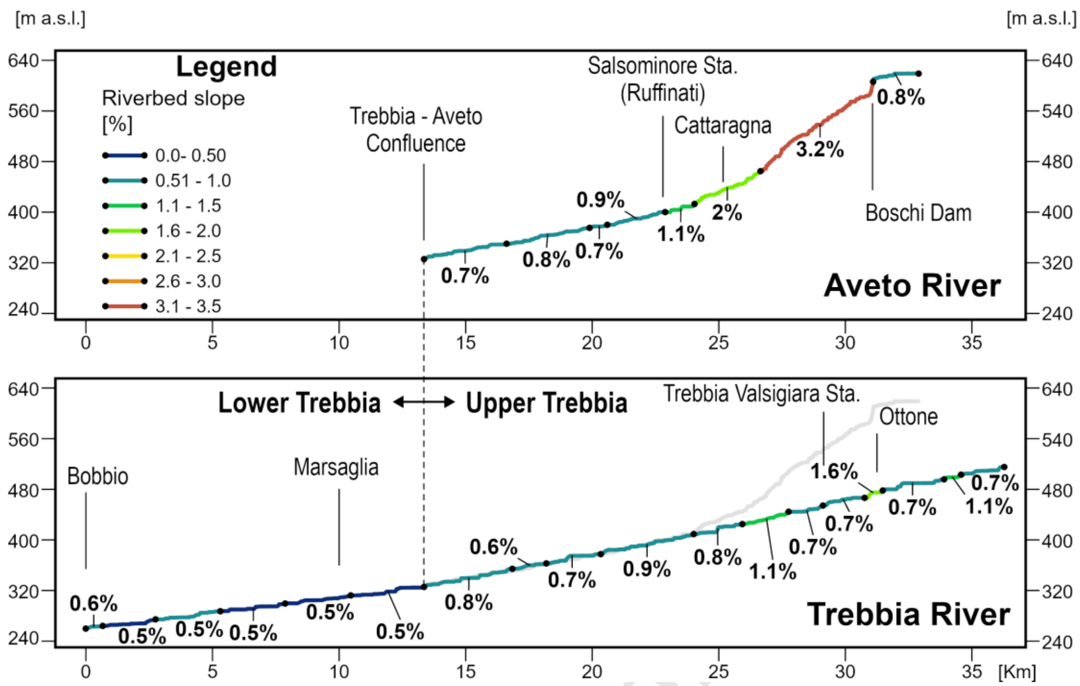


*Figure 3. Longitudinal profiles (Thalweg) of Trebbia River and Aveto River (TAR) system. The color on the profile line indicates the average riverbed slopes on certain sections of the TAR system. The precise slope values are indicated by percentages.*

## *2.4 Debris-flow events of 2015*

On 13–14 September 2015, a ~6-h Mesoscale Convective System (MCS) produced thunderstorm clusters that generated intense rainstorms, with a peak intensity of 82 mm $h^{-1}$ and a total accumulation of 307.4 mm recorded at the Salsominore and Trevia Valsagiara rain-gauge, near the storm core (Figure 1 and Figure 4). The return period of the event was estimated to exceed 100–150 years (Scorpio et al., 2018).

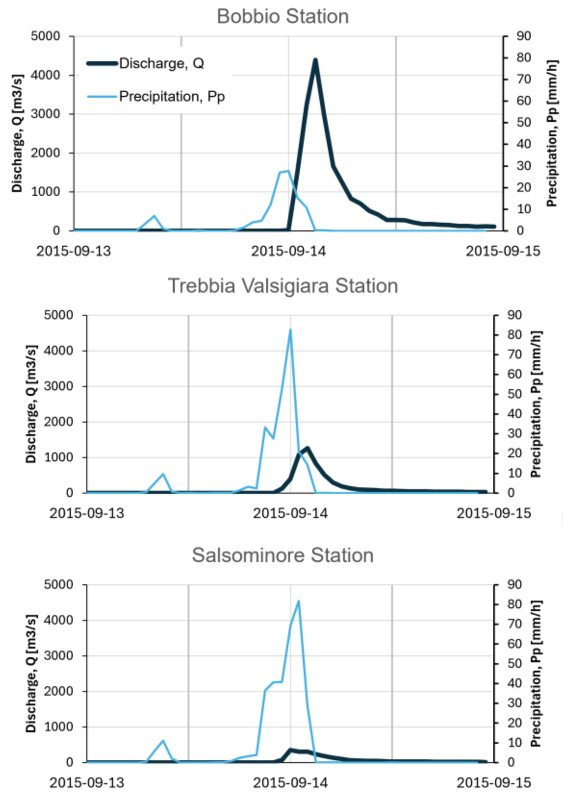


*Figure 4. Hyetographs and hydrographs from the rain and water level gauging stations in the Trebbia–Aveto river system during the events of September 2015 that triggered multiple debris flows. The discharges of these three stations are based on stage measurements (water level); however, since the Trebbia Valsigiara and Salsominore river gauging stations were affected by the debris flow sediment pulses, their records should be considered affected by uncertainty.*

The storm triggered ~110 debris flows, 84 of which occurred within the study area (Ciccarese et al., 2016; Corsini et al., 2019; Ciccarese et al., 2020). The landslide inventory is based on the work of Ciccarese et al. (2020) , which is reported to be built on field surveys and comparisons of pre- and post-event airborne images. The inventory includes debris flows and “debris floods” (Hungr et al., 2001). The spatial distribution of debris-flow initiation closely matched the footprint of the convective storm cluster. Most debris flows were canalized within slope incisions and small headwater creeks draining densely vegetated hillslopes (Figure 5). The source areas primarily consist of rotational slope failures or locations within channels where existing deposits underwent remobilization. The mobilized sediment largely comprised coarse granular debris, along with sandstone and limestone blocks. This material originated from the weathering of weak, heterogeneous rock formations—predominantly Flysch characterized by a high lithic-to-pelite ratio—which occasionally interbeds with clayey shales featuring a block-in-matrix structure. Deposition generally occurred in areas experiencing abrupt transitions in slope gradient or on small debris fans formed where the flows intersected main river networks (Ciccarese et al., 2020).

Post-event surveys across all identified debris flows revealed that a substantial portion of DF-derived sediments remained deposited in slope incisions and small creeks where they were channelized. Nevertheless, a fraction of DF sediments was delivered to the TAR network, collectively producing a debris-flow sediment pulse (DFSP) available for fluvial transport across the river network.

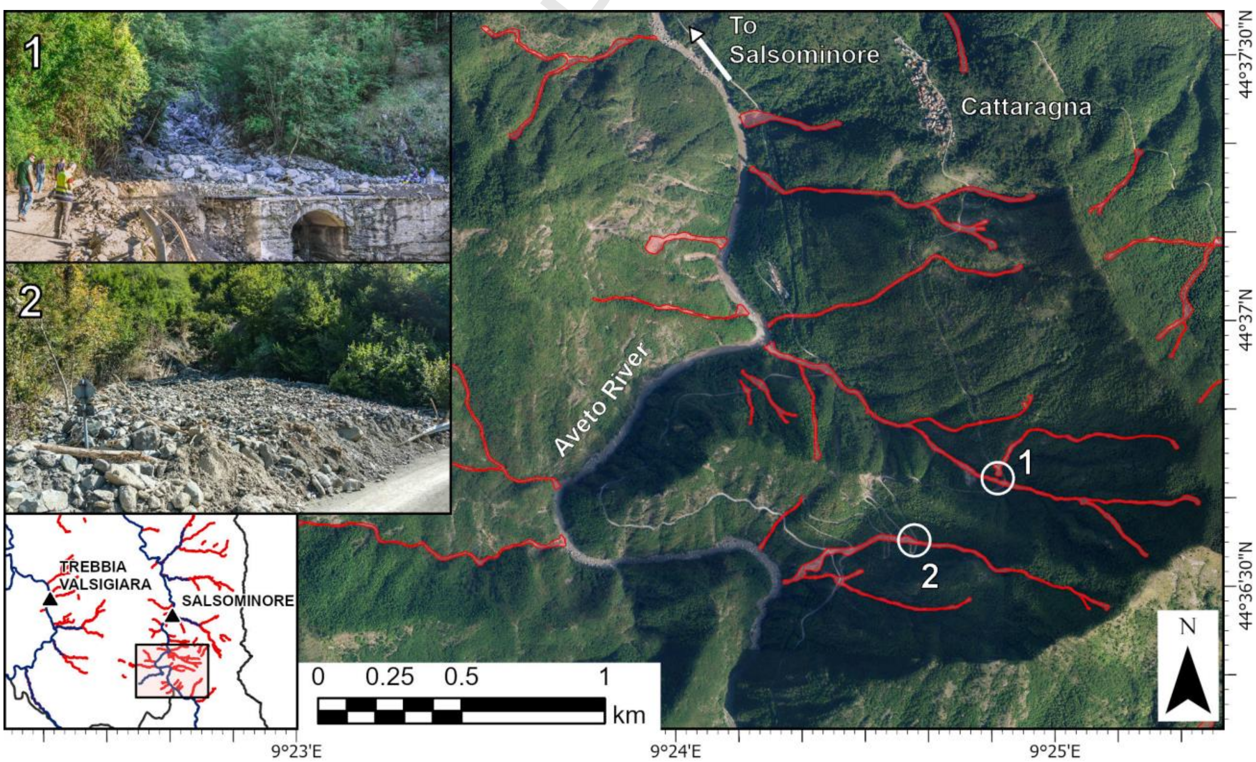

*Figure 5. Mapping of 2015 debris flows affected areas (source area, transport channel, and deposition zone) and some pictures of their sediments. The pictures are not scaled; however, larger blocks are approximately 0.8 $m^3$ to 1 $m^3$ (the deposit vertical height is 1 to 1.2m approximately).*

From a hydrological perspective, on 14 September at the basin outlet (Bobbio hydro-meteorological station), the mean daily discharge of the Trebbia River reached 546.99 $m^3 s^{-1}$. At the same station, the 30-min stage record shows a peak water level of 6.2 m, which—using the station stage–discharge relation—corresponds to an estimated instantaneous peak discharge of ~3,500–4,000 $m^3 s^{-1}$ (Figure 4). The stations of Salsominore and Trebbia Valsigiara also showed a significant increase in the discharge; however, the data seems to be not reliable due to water level sensors being affected by the debris-flow sediment pulses.

## 3 Methodology

### *3.1 D-CASCADE model overview*

D-CASCADE simulates network-scale sediment transport by applying established bed-material transport equations to river reaches—sections of the network with similar hydro-morphological characteristics (e.g., slope, active-channel width)—and iteratively in time. Each reach is parameterized by: slope ($m\ m^{-1}$), length (m), discharge $Q$ ($m^3 s^{-1}$), Manning roughness (n), active-channel width (m), and grain-size distribution, GSD ($D_{16}$,$D_{50}$, $D_{84}$). The model is initialized with a sediment deposit volume per reach and can include external sediment sources and barriers (e.g., landslides, dams), whose effects on the reach-scale sediment budget may be constant or time-varying (Implementation details in Tangi et al., 2022.).

D-CASCADE extends the CASCADE framework (network-scale sediment connectivity) by dynamically routing multiple grain sizes and representing time-dependent disturbances across the entire river network. Further characteristics and limitations of D-CASCADE are commented on in the discussion section.

### *3.2 D-CASCADE inputs*

#### *3.2.1* River-network extraction and reach segmentation

For this study, the river network was extracted from a 5x5 m DEM using the *extract_river_network* routine in the CASCADE toolbox (Tangi et al., 2019). Reaches were created with an average length of ~2 km, yielding a total of 43 reaches (Figure 7). This workflow also returns the mean slope and mean length for each reach. (Background on the DEM-based extraction and stream-graph objects is provided by *TopoToolbox* v2; Schwanghart and Scherler, 2014).

#### *3.2.2* Reaches hydrographs

Reach hydrographs were derived by area-based downscaling of daily average discharges from gauging stations on the Trebbia River basin (Bobbio, Trebbia Valsigiara and Salsominore). Model iterations, therefore, use a daily time step. For consistency across the network, each reach hydrograph was referenced to the observed hydrograph at Bobbio. The downscaling equation has the form:

$$QR_n = J_n \times QB$$

Where the discharge at reach $n$ ($QRn$) is the discharge at Bobbio station ($QB$) multiplied by the scaling factor $J_n$ calculated per reach. Methodological foundations for the area-based downscaling are described in Schmitt et al. (2016). The scaling factors per reach are described in Table 1.

### *3.2.3 Hydraulic roughness*

The Manning roughness coefficient (n) was assigned from published ranges for natural mountain streams, 0.35–0.50 (Table 1), with the exact value depending on boulder content within each reach (Arcement and Schneider, 1989). This coefficient was held constant per reach over all model iterations.

### *3.2.4 Active channel width (Wac)*

The active channel width (*Wac*) is the portion of the channel where sediment entrainment occurs. In this study, *Wac* was treated as a dynamic variable dependent on discharge, *Wac(Q)*. To establish this relation, we compiled six orthomosaic images (2008–2023) and measured *Wac* directly on each image. Five orthophotos were obtained from the Emilia–Romagna geoportal (https://geoportale.regione.emilia-romagna.it/), and one was acquired immediately after the 2015 landslide event. The post-event 2015 orthophoto also provided a constraint on the event maximum width (Wac MAX), inferred from vegetation disturbance and removal/alteration of superficial sediments. Several Wac measurements were made along the TAR system, then averaged to obtain a value per reach on each image.

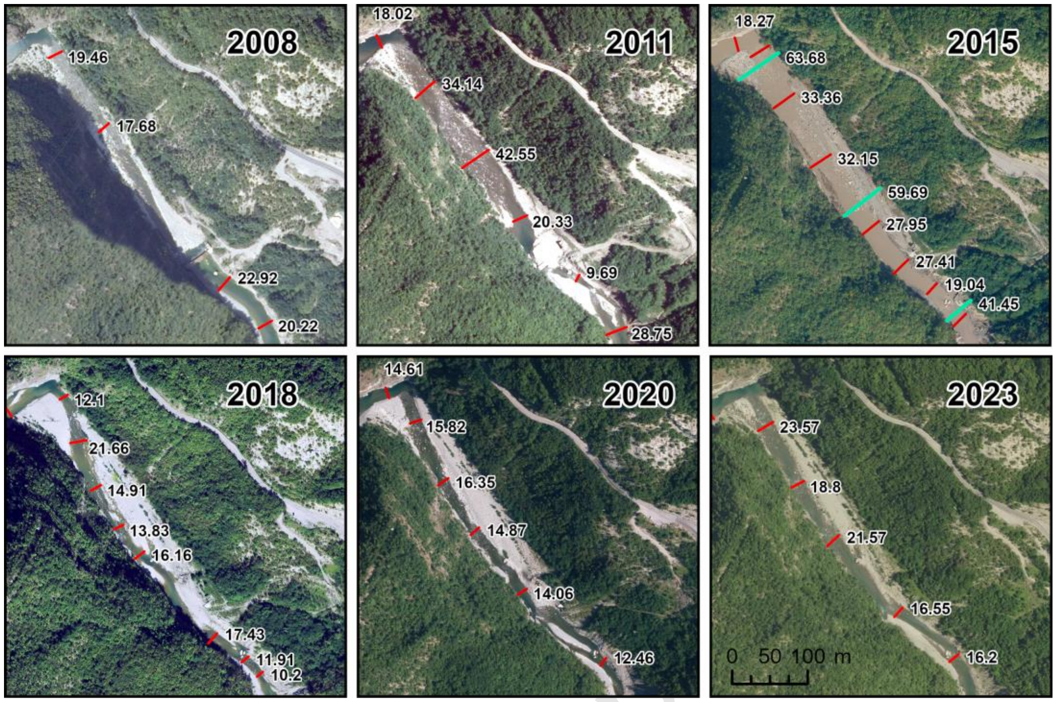


*Figure 6. Example of Wac identification on the set of orthomosaic images from 2008 to 2023. The Wac are marked with red lines and labeled with the length in meters. The image of 2015 also shows the Wac MAX estimation (green lines).*

Because the orthophoto acquisition dates are known, the contemporaneous discharge at each date could be extracted, enabling per-reach regressions between *Wac* and *Q*. For each reach, we fitted a power-law correlation of the form *Wac = a Q^b*, whose parameters are in Table 1. Based on this correlation, daily Wac values were estimated from the daily average discharge for each reach.

### *3.2.5 Grain-size distribution (GSD)*

Reach GSD was obtained by photo-sieving, using digital grain-size recognition applied to drone-derived orthophotos of river bars taken for this work during 2025. The intent was to acquire ≥ 1 orthophoto per reach, where direct access to a site was not possible due to terrain constraints, the orthophoto was taken at the nearest accessible location upstream or downstream of the target reach. Orthophotos were acquired with a DJI Mini 3 Pro (DJI, 2022) flown at ~10 m altitude, yielding an image resolution of ~2.5–3.0 mm $px^{-1}$. This sets a practical detection threshold near 5 mm (≈ 2 pixels). Images were processed in Agisoft Metashape Professional (v1.8.4; Agisoft LLC, 2022) to produce 46 orthorectified mosaics of river bars and landslide deposits, ranging from 10 m×10 m to 80 m ×30 m image size (Figure 6). For each mosaic, 4–10 representative 4 m × 4 m clips (samples) were selected and processed.

The digital photo-sieving algorithm utilized was pyDGS (Buscombe, 2015), which applies a Continuous Wavelet Transform—a mathematical technique that detects repeating spatial patterns across multiple scales (Buscombe, 2013). By analyzing variations in the pixel intensity of light and shadow, the algorithm estimates the relative volumetric proportion of different grain sizes without the need to delineate individual grains. From this distribution, standard grain-size percentiles (from $D_5$ to $D_{95}$) are derived via linear interpolation. The $D_{16}$, $D_{50}$, and $D_{84}$ were extracted and used as the reach GSD descriptors of the initial sediment deposit of the main channel of the TAR system (Figure 6). The values of $D_{16}$, $D_{50}$ and $D_{84}$ per reach can be found in Table 1. PyDGS is straightforward to implement, computationally efficient, and provides accuracy suitable for the purposes of this study. It must be noted, however, that image-based methods are strictly bound by optical resolution. Therefore, the resulting distribution is inherently biased against the fine-grained fraction (e.g., sub-pixel matrix material), which artificially truncates the lower tail of the grain-size distribution.

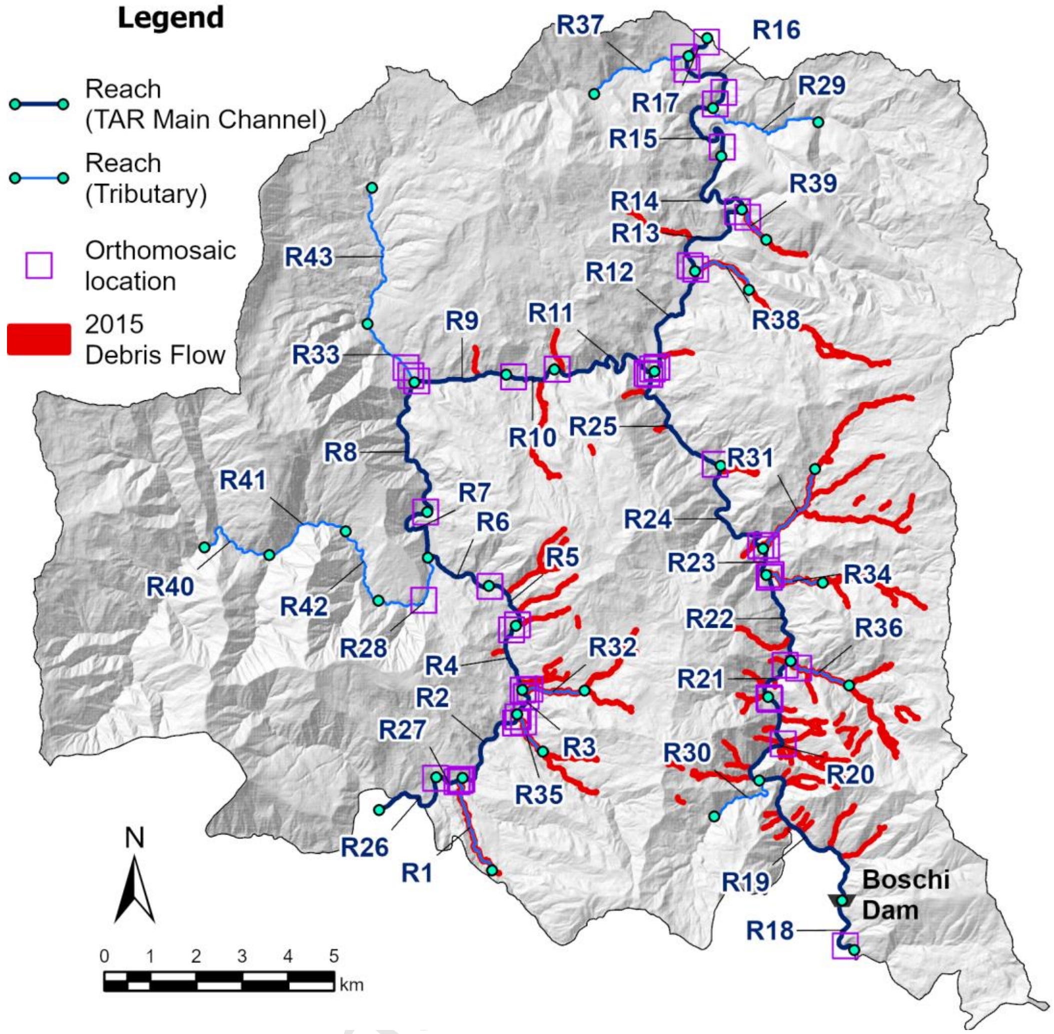


*Figure 7. Reach segmentations of the river network of the TAR system and orthomosaic location.*

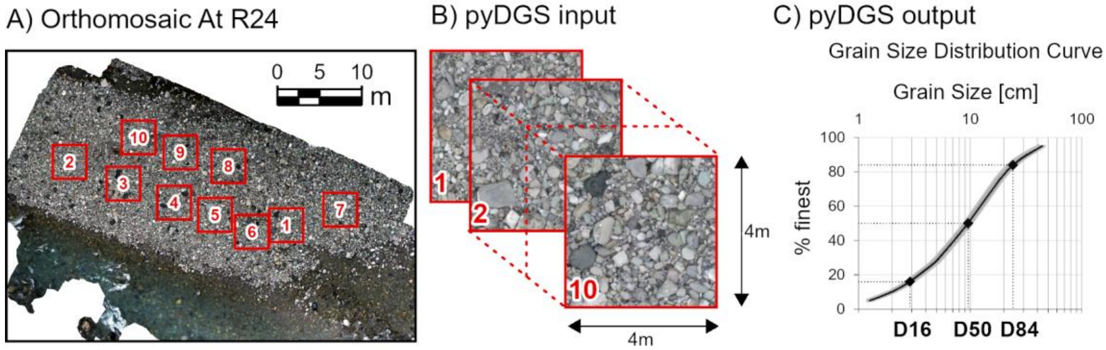


*Figure 8. Example of GSD extraction from Orthomosaic. A) Depending on the size of the Orthomosaic, up to ten small patches are selected that represents the sediments of the river bars. B) All the patches are extracted as individual georeferenced images and input into pyDGS. C) pyDGS provides the GSD for each image, and the resulting curve is generated from the average.*

| River Network Section | Reach R | Length [km] | Slope [%] | Drainage Area [km²] | Q Scaling factor, Jn | Manning Coef [] | Wac Max average [m] | Wac Parameters Wac = a x Q^b a | b | GSD D16 | D50 | D84 | Initial Sed. Deposit [m³] x10 ^3 | Debris Flow Sediment pulse, DFSP per reach [m³] x10 ^3 |
|---|---|---|---|---|---|---|---|---|---|---|---|---|---|---|
| Tributary | 1 | 2.60 | 8.6 | 7.4 | 0.063 | 0.035 | 24.5 | 3.705 | 0.361 | 0.045 | 0.178 | 0.483 | 0 | 28.58 |
| | 2 | 2.42 | 0.7 | 190.6 | 0.432 | 0.035 | 46.5 | 15.415 | 0.156 | 0.031 | 0.094 | 0.227 | 337.593 | 0 |
| | 3 | 0.71 | 1.6 | 206.0 | 0.447 | 0.035 | 82.3 | 11.238 | 0.262 | 0.027 | 0.074 | 0.167 | 174.688 | 0 |
| | 4 | 1.65 | 0.7 | 213.7 | 0.458 | 0.035 | 63.5 | 16.166 | 0.184 | 0.035 | 0.109 | 0.252 | 314.582 | 11.59 |
| | 5 | 1.35 | 0.7 | 217.1 | 0.463 | 0.035 | 52.3 | 13.769 | 0.185 | 0.036 | 0.112 | 0.264 | 212.013 | 12.31 |
| | 6 | 1.83 | 1.1 | 221.1 | 0.467 | 0.035 | 71.7 | 13.141 | 0.230 | 0.019 | 0.056 | 0.128 | 393.521 | 0 |
| | 7 | 1.92 | 0.8 | 274.9 | 0.533 | 0.035 | 110.0 | 12.739 | 0.289 | 0.025 | 0.071 | 0.159 | 845.209 | 0 |
| | 8 | 3.68 | 0.9 | 276.8 | 0.538 | 0.035 | 61.0 | 16.490 | 0.175 | 0.025 | 0.071 | 0.159 | 672.833 | 0 |
| | 9 | 2.15 | 0.7 | 313.2 | 0.578 | 0.035 | 52.2 | 17.766 | 0.147 | 0.028 | 0.080 | 0.182 | 336.349 | 2.38 |
| | 10 | 1.35 | 0.6 | 318.8 | 0.585 | 0.035 | 82.9 | 15.810 | 0.216 | 0.023 | 0.069 | 0.160 | 334.712 | 21.51 |
| | 11 | 3.49 | 0.8 | 326.1 | 0.595 | 0.035 | 64.8 | 13.399 | 0.207 | 0.029 | 0.080 | 0.169 | 678.137 | 6.37 |
| | 12 | 2.89 | 0.5 | 585.4 | 0.843 | 0.035 | 150.0 | 19.220 | 0.264 | 0.022 | 0.065 | 0.153 | 1736.649 | 5.09 |
| | 13 | 2.59 | 0.5 | 599.8 | 0.855 | 0.035 | 100.0 | 18.590 | 0.220 | 0.014 | 0.035 | 0.076 | 777.790 | 10.27 |
| Main channel | 14 | 2.57 | 0.5 | 613.4 | 0.865 | 0.035 | 87.8 | 14.485 | 0.226 | 0.018 | 0.049 | 0.109 | 1127.034 | 0 |
| | 15 | 2.56 | 0.5 | 617.2 | 0.868 | 0.035 | 86.2 | 25.465 | 0.155 | 0.015 | 0.039 | 0.089 | 660.882 | 0 |
| | 16 | 2.08 | 0.5 | 640.1 | 0.887 | 0.035 | 92.7 | 21.823 | 0.179 | 0.023 | 0.067 | 0.156 | 385.817 | 0 |
| | 17 | 0.67 | 0.6 | 652.0 | 0.897 | 0.035 | 120.0 | 23.767 | 0.202 | 0.018 | 0.050 | 0.115 | 160.165 | 0 |
| | 18 | 1.60 | 0.8 | 169.2 | 0.398 | 0.035 | 53.2 | 15.531 | 0.171 | 0.019 | 0.052 | 0.120 | 170.240 | 0 |
| | 19 | 4.46 | 3.2 | 172.0 | 0.410 | 0.050 | 35.7 | 11.132 | 0.169 | 0.031 | 0.094 | 0.227 | 158.927 | 25.63 |
| | 20 | 2.61 | 2.0 | 191.8 | 0.431 | 0.050 | 34.8 | 13.293 | 0.139 | 0.034 | 0.099 | 0.238 | 90.835 | 49.71 |
| | 21 | 1.16 | 1.1 | 197.2 | 0.437 | 0.035 | 39.9 | 14.128 | 0.151 | 0.034 | 0.090 | 0.200 | 92.483 | 1.42 |
| | 22 | 2.27 | 0.9 | 209.7 | 0.454 | 0.035 | 56.9 | 16.479 | 0.175 | 0.027 | 0.084 | 0.206 | 259.034 | 8.63 |
| | 23 | 0.70 | 0.7 | 220.0 | 0.465 | 0.035 | 66.0 | 12.885 | 0.226 | 0.026 | 0.081 | 0.198 | 92.157 | 0 |
| | 24 | 3.28 | 0.8 | 233.9 | 0.487 | 0.035 | 63.5 | 15.276 | 0.198 | 0.024 | 0.073 | 0.173 | 416.589 | 8.30 |
| | 25 | 3.27 | 0.7 | 241.7 | 0.496 | 0.035 | 68.5 | 15.377 | 0.203 | 0.026 | 0.079 | 0.195 | 447.534 | 0 |
| | 26 | 2.19 | 0.7 | 170.9 | 0.403 | 0.035 | 44.3 | 17.150 | 0.136 | 0.024 | 0.067 | 0.147 | 291.113 | 0 |
| | 27 | 0.68 | 1.1 | 177.6 | 0.411 | 0.035 | 44.4 | 15.639 | 0.152 | 0.031 | 0.094 | 0.227 | 90.807 | 0 |
| | 28 | 2.29 | 2.0 | 46.4 | 0.187 | 0.035 | 29.4 | 6.092 | 0.241 | 0.019 | 0.051 | 0.115 | 0 | 0 |
| | 29 | 3.13 | 6.6 | 17.7 | 0.107 | 0.040 | 15.0 | 2.960 | 0.273 | 0.022 | 0.072 | 0.180 | 0 | 0 |
| | 30 | 1.95 | 13.0 | 5.1 | 0.051 | 0.050 | 9.7 | 3.551 | 0.195 | 0.045 | 0.178 | 0.483 | 0 | 0 |
| | 31 | 2.42 | 12.5 | 5.0 | 0.067 | 0.035 | 18.5 | 4.085 | 0.286 | 0.023 | 0.067 | 0.153 | 0 | 69.28 |
| | 32 | 1.61 | 10.5 | 5.9 | 0.054 | 0.035 | 26.6 | 3.712 | 0.381 | 0.032 | 0.093 | 0.222 | 0 | 40.76 |
| | 33 | 1.80 | 4.4 | 26.0 | 0.133 | 0.035 | 11.1 | 4.804 | 0.142 | 0.017 | 0.047 | 0.105 | 0 | 0 |
| | 34 | 1.63 | 10.7 | 5.0 | 0.050 | 0.040 | 16.2 | 3.616 | 0.295 | 0.020 | 0.052 | 0.113 | 0 | 68.23 |
| Tributary | 35 | 1.14 | 5.9 | 5.5 | 0.051 | 0.035 | 20.6 | 3.922 | 0.319 | 0.027 | 0.085 | 0.210 | 0 | 42.40 |
| | 36 | 1.63 | 7.3 | 7.1 | 0.063 | 0.040 | 32.9 | 4.378 | 0.378 | 0.018 | 0.049 | 0.110 | 0 | 81.54 |
| | 37 | 2.69 | 8.2 | 6.6 | 0.064 | 0.035 | 18.4 | 2.788 | 0.355 | 0.018 | 0.049 | 0.112 | 0 | 0 |
| | 38 | 1.68 | 8.8 | 5.1 | 0.052 | 0.035 | 18.6 | 3.777 | 0.309 | 0.013 | 0.030 | 0.058 | 0 | 75.01 |
| | 39 | 0.95 | 9.4 | 5.0 | 0.049 | 0.035 | 19.8 | 1.315 | 0.527 | 0.000 | 0.072 | 0.180 | 0 | 6.78 |
| | 40 | 2.29 | 3.1 | 26.4 | 0.137 | 0.040 | 11.6 | 6.322 | 0.103 | 0.019 | 0.051 | 0.115 | 0 | 0 |
| | 41 | 2.29 | 2.4 | 32.4 | 0.158 | 0.035 | 21.2 | 6.830 | 0.179 | 0.019 | 0.051 | 0.115 | 0 | 0 |
| | 42 | 2.29 | 2.4 | 41.9 | 0.176 | 0.035 | 34.1 | 6.071 | 0.259 | 0.019 | 0.051 | 0.115 | 0 | 0 |
| | 43 | 3.61 | 4.5 | 6.5 | 0.087 | 0.040 | 7.9 | 2.764 | 0.202 | 0.017 | 0.047 | 0.105 | 0 | 0 |

*Table 1. D-CASCADE inputs per reach. The drainage area is calculated with outlet at the end of the reach.  Tributaries are assumed with no  initial sediment.*

### *3.3 Model setup*

#### *3.3.1 Simulation period and time step*

The simulation covers 1 September 2015 to 12 December 2024, i.e., slightly over 9 years, driven by daily mean discharges available at the Bobbio station. The model time-step is 1 day, consistent with the temporal resolution of the hydrological downsizing and the D-CASCADE input structure.

#### *3.3.2 River-network configuration*

The river network comprises 43 reaches: 18 in the Trebbia River, 8 in the Aveto River, and the remaining 17 representing tributaries to both rivers. Reach attributes (slope, length, hydraulics) follow the D-CASCADE/CASCADE reach parametrization used for network-scale routing.

#### *3.3.3 Sediment transport capacity formulas and Fractional Computation Method*

To model mixed-size sediment, D-CASCADE categorizes riverbed material into size classes based on the Krumbein (φ) logarithmic scale (Krumbein and Sloss, 1963). The number and width of these classes are user-defined. For this study, we defined 12 classes ranging from φ = 3.5 (~0.088 mm, very fine sand) to φ = -8.5 (~362 mm, boulders) at intervals of 1 φ. We also included two boundary classes to capture sediment finer than 0.088 mm and coarser than 362 mm. The representative diameter for each regular class is set to its upper bound; for example, the class ranging from φ = -1.5 to -2.5 is assigned a diameter of φ = -2.5 (~5.6 mm). As a special case, the open-ended coarsest class (>362 mm) is assigned an arbitrary representative diameter of φ = -9.5 (~724 mm).

D-CASCADE converts the D16, D50, and D84 percentiles (extracted via digital photo-sieving) into a grains-size frequency distribution by fitting the data to a Rosin distribution curve (Shih and Komar, 1990). Using the volume of each class, the model iteratively applies sediment transport capacity equations. We utilized six equations available within the framework: Parker and Klingeman (1982), Wilcock and Crowe (2003), Engelund and Hansen (1967), Yang (1984), Wong and Parker (2006), and Ackers and White (1973).

While the Parker and Klingeman and Wilcock and Crowe equations compute fractional transport natively, the remaining four calculate total sediment transport capacity. To partition this total load, we applied the Transport Capacity Fraction (TCF) approach (Wu et al., 2003). The TCF approach is particularly advantageous for widely graded gravel-bed rivers because it explicitly accounts for extreme hiding and exposure effects. In these morphologies, finer fractions are sheltered within the interstitial matrix of larger clasts, while coarse fractions experience disproportionate flow exposure (Wilcock, 2001; Bui et al., 2019).

Although all six equations were applied to allow cross-comparison of results, Wilcock-Crowe (WC) was considered a priori the most theoretically suitable formulation for the TAR system conditions, based on the following characteristics. As a surface-based bedload transport model developed for mixed sand-gravel rivers, WC incorporates the full surface GSD in estimating transport (de Linares and Belleudy, 2007; Cui, 2007; Gaeuman et al., 2009; Vazquez and Menendez, 2015; Cordier et al., 2016; Jones et al., 2025) and is naturally coupled to the active-layer concept (Church and Haschenburger, 2017) implemented in D-CASCADE. In the current setup, the DFSP was incorporated into D-CASCADE as part of the active layer, representing material immediately available for mobilization. The remaining equations present additional limitations relative to the TAR system conditions: Engelund-Hansen and Ackers-White were calibrated using uniform sand and fine gravel under flume conditions, placing the coarser fractions of the TAR bed material and DFGSP outside their valid calibration ranges; Parker-Klingeman, while applicable to gravel-bed rivers, is a subsurface-based formulation calibrated exclusively for flows capable of fully mobilizing the armor layer (Monsalve et al., 2020), a condition not representative of the full flow range modelled in D-CASCADE; and Wong-Parker is strictly applicable to plane-bed conditions, which are not representative of a gravel-bed river subject to episodic sediment pulse inputs. For these reasons, Wilcock-Crowe was adopted as the primary equation for the TAR system in this study, while all six equations were retained for the initial cross-comparison of results.

#### *3.3.4 Sediment sources and initial conditions*

Two sources of sediment are represented within the model: initial deposit volumes already present in the main channel and the discrete sediment inputs generated by the 2015 debris-flow events (referred to as debris-flow sediment pulse, DFSP).

**Initial deposit volumes per reach (main channel of the TAR system)**

Initial deposit volumes for the main channel of the TAR system were calculated as the product of the average deposit thickness, reach length, and maximum active channel width (Wac MAX). The average deposit thickness for each reach was derived from cross-sectional transects extracted from a 1 m × 1 m LiDAR DEM, augmented by an estimated 1 to 2 m of subsurface sediment beneath the active riverbed (Figure 9). The Wac MAX represents the channel width observed during the 2015 debris-flow triggering storm, which was interpreted from orthophotos generated a few days after the events.

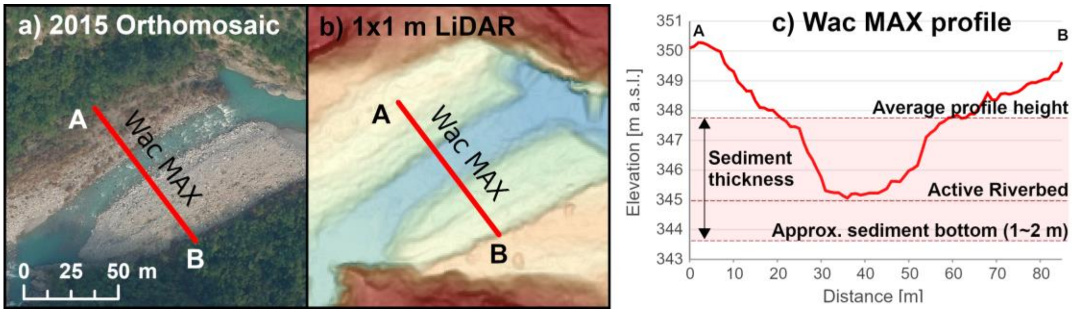


*Figure 9. Sediment thickness estimation example. a) extraction of the maximum active channel width (Wac MAX) from a rectified orthomosaic acquired a few days after the 2015 DF event. b) 1m x 1 m liDAR-derived DTM used to generate the Wac MAX cross-sectional profile. c) Wac MAX profile showing the estimation of sediment thickness. Representative sediment thickness values were extracted along the reach, averaged, and multiplied by the reach length to obtain the sediment volume per reach.*

Main-channel tributaries (i.e., tributary reaches) were initialized with no sediment (Table 1). The fluvial morphologies of these tributaries (i.e., cascade and step-pool systems) are characterized by lower sediment transport power throughout the year than the main channel. Cascade and step-pool channels typically dissipate flow energy over and around large clasts, maintain high transport-capacity-to-supply ratios, and are resilient to changes in discharge and supply except during infrequent, high-magnitude events (Montgomery and Buffington, 1997; Church and Zimmermann, 2007). Bed material in such reaches is immobile most of the time, becoming mobile only under extreme conditions (e.g., ≳100-year events) when armor or step structures are partially undermined. This is consistent with observations that stochastic sediment pulses from hillslope failures often accumulate in low-order channels for years to centuries, transferred intermittently downstream by debris flows rather than by routine floods (Benda and Dunne, 1997). Check dams installed along many small streams in the basin further limit bedload conveyance by fixing bed profiles and trapping sediment, reducing peak bedload and volumes transported during individual events (Piton and Recking, 2017). Small, continuous hillslope supplies were excluded from both scenarios because they are minor relative to DFSP inputs. Dense vegetation cover on Trebbia hillslopes (Ciccarese et al., 2020) further supports this simplification by decoupling slopes from channel bedload under normal hydrologic conditions, with structurally disconnected or only functionally connected sources contributing little to the reach-scale bedload budget except under extremes (Fryirs, 2012).

**2015 Debris-flow sediment pulse volumes and GSD**

As described in Section 2.4, only a fraction of the total DF-derived sediments from the 2015 events entered the reaches of the TAR network (Figure 7) and became available for fluvial transport, with the remainder deposited on slopes or along minor creeks. In the absence of direct measurements, a conservative estimate of the DFSP volume was made as follows.

The total volume of DF-mobilized debris was estimated by multiplying the mapped planform area of each individual DF-affected area (based on mapping by Ciccarese et al., 2020; Figure 5 andFigure 7) by a mean vertical thickness, a method shown to be suitable for shallow mass movement processes (Jaboyedoff et al., 2020). Here, a representative thickness of 1 m was adopted as a conservative, expert-based estimate informed by post-event field observations of DF deposits. From this total volume estimate, the DFSP volume entering the TAR network was estimated by assuming that 50% of the total DF-mobilized debris volume reached the TAR network.

For implementation in D-CASCADE, DFSP per reach (Table 1) was calculated by aggregating the previously estimated fractional volumes of all individual DF events entering a given reach, regardless of their specific entry point along the reach. These estimated DFSP per reach were treated as discrete, single-time-step pulses (one day).

The grain-size distribution (GSD) of DFSP was assumed uniform across DF events, given that all flows shared the same geological and geomorphological setting and field comparisons of deposits supported this assumption. Using the digital grains-size recognition method applied to DF-derived deposits, the grains-size percentiles for DFSP are defined as $D_{16}$= 0.0179 m, $D_{50}$ = 0.0486 m, $D_{84}$ = 0.1096 m.

#### *3.3.5* Upstream sediment supply

Upstream boundary conditions were specified separately for the Trebbia and Aveto rivers because of their contrasting controls. In the Trebbia River, reaches 26 and 27 were assigned an initial channel-stored sediment volume. During the modeled period, mobilization of this in-channel storage is expected to partially or fully meet the upstream sediment influx, thereby limiting the need to prescribe additional supply at the domain boundary. In the Aveto River, reach 19 is immediately downstream of Boschi Dam (Figure 7). Because the dam operation data were unavailable, we adopted a sediment-starved boundary downstream of the dam—assuming negligible bed-material transfer across the structure—while allowing water flow. This configuration reflects common downstream effects of sediment trapping by reservoirs and provides a conservative representation in the absence of flushing or sediment-release events.

#### *3.3.6 Scenario-based comparison.*

System response to the 2015 debris flows was assessed through a counterfactual, scenario-based analysis. Two scenarios were compared: a 'With-DFSP' scenario, which includes the debris flow sediment pulse inputs, and a baseline 'No-DFSP' scenario that excludes them. Using the sediment transport capacity equations implemented in D-CASCADE (Table 2), the DFSP was tracked through the TAR river network as the difference in sediment volume between scenarios (With-DFSP minus No-DFSP). This difference was computed at each time step and cumulatively over the full study period, both at the reach scale and as total sediment export at the basin outlet. This counterfactual subtraction is a standard attribution approach in network-scale sediment-connectivity studies and has been used to evaluate the impacts of disturbances and management strategies (Schmitt et al., 2016; Schmitt et al., 2018; Tangi et al., 2023).

All routing and capacity computations employ the transport-capacity routines available in D-CASCADE (Tangi et al., 2022), consistent with the CASCADE framework and its reach-scale hydraulics and connectivity (Schmitt et al., 2016; Tangi et al., 2019).

# 4 Results

## *4.1 DFSP exports*

We first ran D-CASCADE using all sediment-transport equations available in the package and compared their outcomes in terms of total sediment exports at the study area outlet (Bobbio St.) over the studied period (2015–2024) for both scenarios (With-DFSP and No-DFSP). The inter-scenario difference in exported volume — that is, the With-DFSP minus No-DFSP difference — was then taken as the total DFSP exported (output) from the study area. This exported volume was subsequently compared with the DFSP input, estimated at 562,756 $m^3$, to assess the fraction of the initial sediment pulse evacuated from the basin over the study period and the volume of sediment pulse that remains within the study area (Table 2).

*Table 2. Sediment volumes exported at the basin outlet (Bobbio St.) over the study period (2015–2024) for each transport equation under both scenarios (With-DFSP and No-DFSP). The DFSP exported at the outlet represents the inter-scenario difference (With-DFSP minus No-DFSP) and is expressed as an absolute volume and as a percentage of the total DFSP input.*

| Sediment Transport Equations | Total sed. export **With-DFSP** [m³] | Total sed. export **No-DFSP** [m³] | DFSP exported at outlet [m³] | DFSP exported [%] of total DFSP input | DFSP storage in the study area [m³] |
|---|---|---|---|---|---|
| PARKER-KLINGEMAN | 970,660 | 915,100 | 55,560 | 9.87 | 507,196 |
| **WILCOCK-CROWE** | **145,168** | **139,941** | **5,227** | **0.93** | **557,529** |
| ENGELUND-HANSEN | 115,872 | 114,522 | 1,350 | 0.24 | 561,406 |
| YANG | 4,761,395 | 4,806,458 | -45,063 | -8.01 | 607,819 |
| WONG-PARKER | 364,204 | 361,612 | 2,592 | 0.46 | 560,164 |
| ACKERS-WHITE | 66,958 | 66,770 | 188 | 0.03 | 562,568 |

Across transport equations and over the ~10-year study period, the fraction of DFSP exported from the study area is small: below 1% for all equations except Parker-Klingeman, which approaches ~10%. The Yang equation is excluded from this comparison and further analysis because it produced a negative DFSP export value, indicating greater sediment export under the No-DFSP than under the With-DFSP scenario. This physically inconsistent result is attributed to the tendency of the Yang equation to overestimate transport capacity for coarse sediments beyond its calibration range (Yang, 1973), which is particularly problematic in steep, coarse-grained mountain channels such as those of the TAR system. For all remaining equations, the vast majority of the DFSP therefore remains stored within the basin over the study period.

### *4.2 Spatial distribution of DFSP stored*

Because most DFSP is stored inside the study area, we next examined where it accumulates. By calculating the inter-scenario differential of the total sediment content on each reach, we obtained the DFSP storage fraction on a reach by the end of the study period. Figure 10 shows that most equations agree on the general spatial pattern of DFSP storage. The two primary storage locations are Reach 13 and around Reach 24, with a secondary accumulation zone around Reach 4.

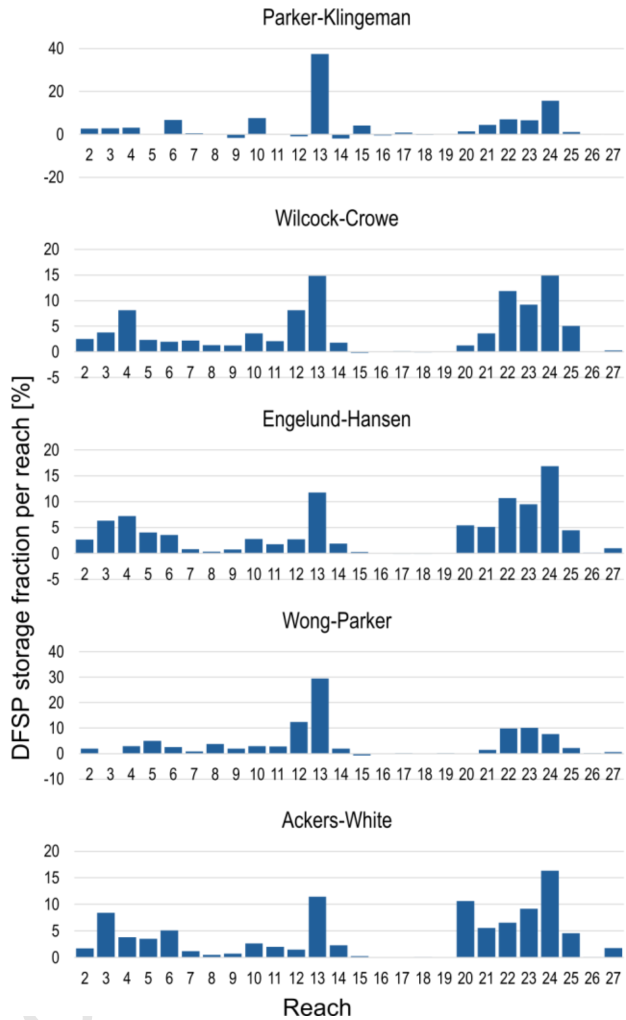


*Figure 10. DFSP storage fractions per reach, calculated using each of the evaluated sediment transport capacity equations.*

Since most equations yield broadly consistent spatial patterns of DFSP storage, the choice of a single equation for subsequent analysis does not fundamentally alter the spatial conclusions. Wilcock-Crowe was therefore selected for all subsequent analysis, given its theoretical suitability for the TAR system conditions as discussed in Section 3.3.3. Figure 11 and Figure 12 show the spatial distribution of DFSP storage across the TAR network based on the Wilcock-

Crowe results.

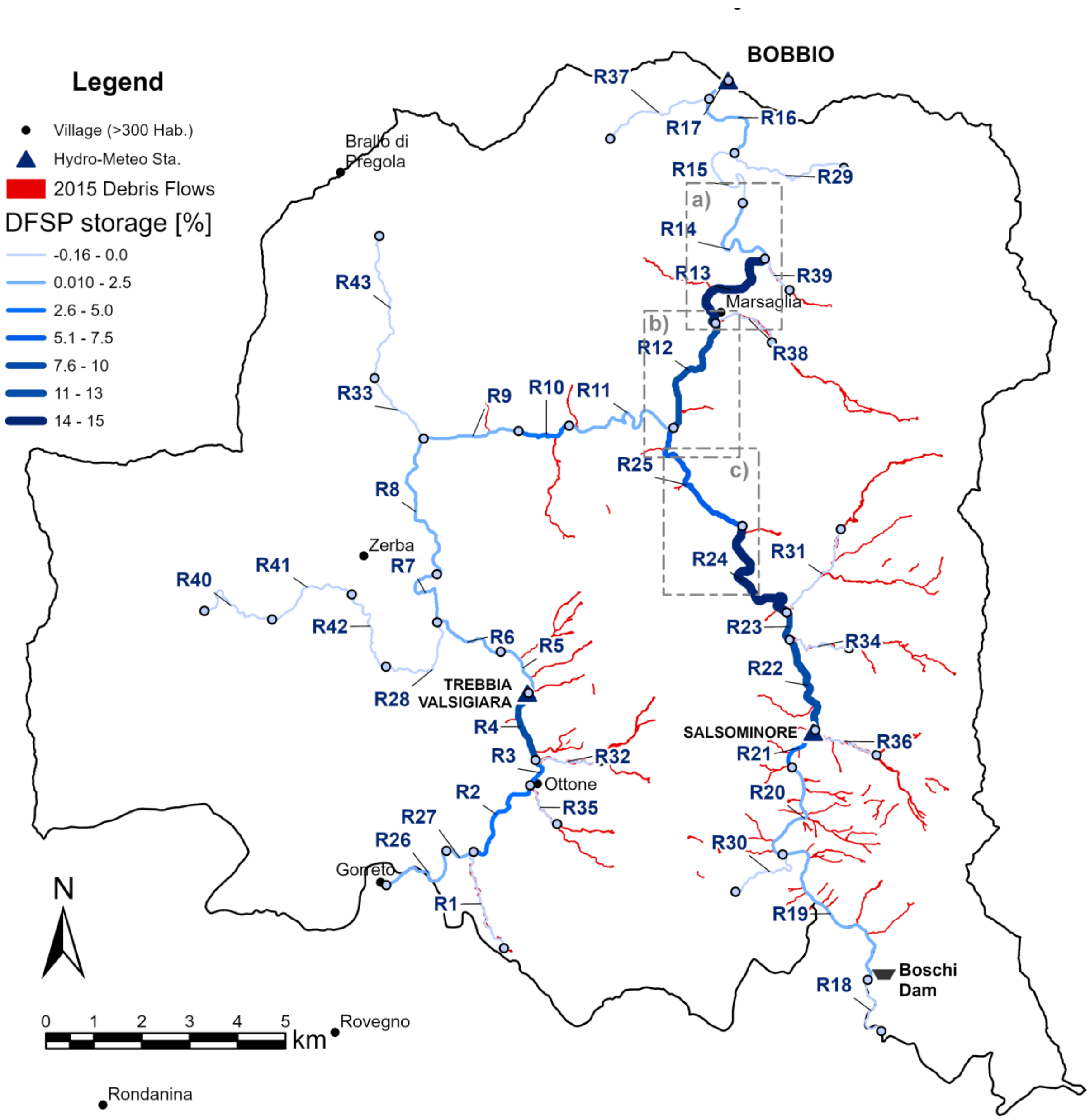


*Figure 11. Spatial distribution of DFSP storage per reach in the study area by the end of the study period (Sept 2015 - Dec. 2024). The segmented rectangles "a)", "b)" and "c)" refer to the location of the detailed images in Figure 13.*

*Table 3. Detailed DFSP storage per reach by the end of the study period (Sept 2015 - Dec. 2024).*

| Reach, R | 1 | 2 | 3 | 4 | 5 | 6 | 7 | 8 | 9 | 10 | 11 | 12 | 13 | 14 |
|---|---|---|---|---|---|---|---|---|---|---|---|---|---|---|
| DFSP Storage [%] | 0 | 2.51 | 3.77 | 8.14 | 2.34 | 1.97 | 2.22 | 1.02 | 1.23 | 3.52 | 2.18 | 8.00 | 14.97 | 1.88 |
| **Reach, R** | **15** | **16** | **17** | **18** | **19** | **20** | **21** | **22** | **23** | **24** | **25** | **26** | **27** | **28 - 43** |
| DFSP Storage [%] | -0.16 | 0.07 | 0.09 | -0.02 | 0.02 | 1.25 | 3.61 | 11.89 | 9.22 | 14.90 | 5.05 | 0.01 | 0.26 | 0 |

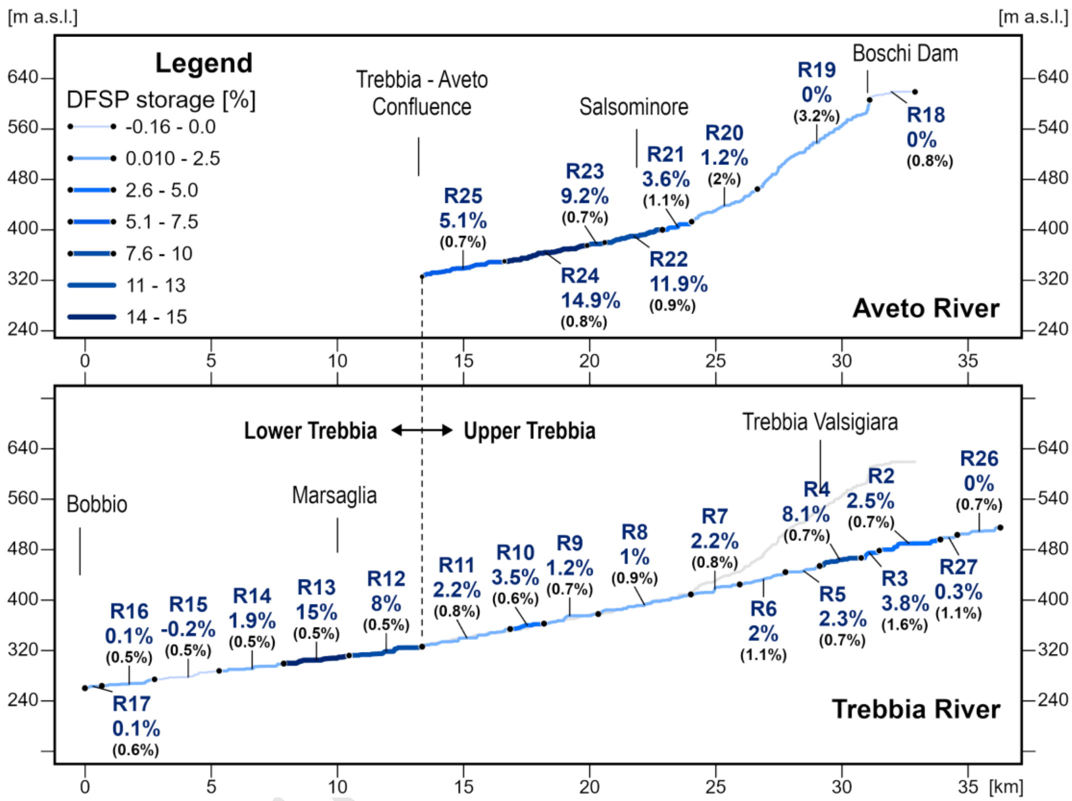


*Figure 12. DFSP storage distribution per reach on a longitudinal profile (Thalweg) of the TAR system by the end of the study period (Sept. 2015 - Dec. 2024). Under the reach labels, the percentage of the DFSP storage in the corresponding reach is indicated. The percentage in parentheses indicates the average riverbed slope of the reach.*

Figure 11 shows large DFSP storage immediately downstream of DF sources by the end of the study period. In the upper Trebbia River, the largest deposit is in reach 4, directly downstream of reaches 32 and 35, which received major DF inputs. In the Aveto River, the largest deposits are found in reaches 22, 23, and 24, downstream of reaches 36, 34, and 31, which received major DF inputs. A downstream mobilization of DFSP from these large storage zones is observed. Below reach 4, reaches 5–9 together accumulate 8.7% of DFSP. Below reach 24, reaches 25, and 12 accumulate 5.1% and 8.0%, respectively, without receiving substantial direct DF input — indicating secondary re-entrainment and redeposition of DFSP (Table 3).

Figure 12 suggests that the riverbed slope acts as a secondary control on DFSP storage. The reaches with the highest slopes, reaches 19 and 20, receive a combined 14% of DFSP directly — slightly more than 75,000 $m^3$ (Table 1) — yet only 1.2% of DFSP remains stored by the end of the study period, entirely within reach 20. The DFSP evacuated from these reaches appears to contribute to the large storage zones in reaches 21–24 downstream, where the reduced riverbed slope promotes deposition. A similar process may occur at the confluence of the Trebbia and Aveto rivers. Downstream of the confluence, the lower Trebbia exhibits a slight but perceptible reduction in riverbed slope relative to the upper Trebbia and Aveto rivers, which may contribute to the large DFSP storage observed in reach 12 — a reach that does not receive significant direct DF input. An additional morphological factor contributing to the large DFSP storage in reaches 12 and 13 is the widening of the Trebbia valley.

D-CASCADE does not directly account for valley width, but does so indirectly through the active channel width, Wac(Q), as illustrated by the WacMAX in Figure 13 (segmented red line). While a wide valley does not necessarily produce a wide channel — as other factors such as discharge, sediment supply, and bank resistance also control channel width — a narrow valley imposes a hard upper limit on channel width, since the channel cannot exceed the valley floor width. This asymmetric relationship is broadly consistent with observations in the TAR system, where valley narrowing in the lower Trebbia River coincides with a progressive reduction in Wac(Q). However, since Wac is calculated as a reach average, localized valley constrictions within a reach may not be adequately represented. Figure 13b shows the terminal sections of reaches 11 and 25 with WacMAX values of 47 m and 57 m, respectively, increasing to 158 m in reach 12.

Beyond reach 12, the average WacMAX per reach progressively decreases from 150 m in reach 12 to 100 m in reach 13, and further to 88 m and 86 m in reaches 14 and 15, respectively (Table 1). This progressive reduction in WacMAX is broadly consistent with a narrowing of the Trebbia valley, although reach-averaged width values do not perfectly capture localized valley constrictions; together, these factors appear to produce a funnel effect that may limit further DFSP transport downstream, contributing to the low DFSP storage observed from reaches 15 to 17. This funnel effect is likely underrepresented in our D-CASCADE setup, as localized valley constrictions are averaged out at the reach scale. This is the case for reach 25, which contains localized constrictions that narrow the channel but are insufficient to reduce the reach-averaged width significantly (Figure 13c). A similar situation occurs between reaches 14 and 15, where the valley constricts, limiting the channel width to 49 m (Figure 13a). A finer reach discretization isolating these localized valley constrictions would enable D-CASCADE to better account for their effect on sediment transport and deposition.

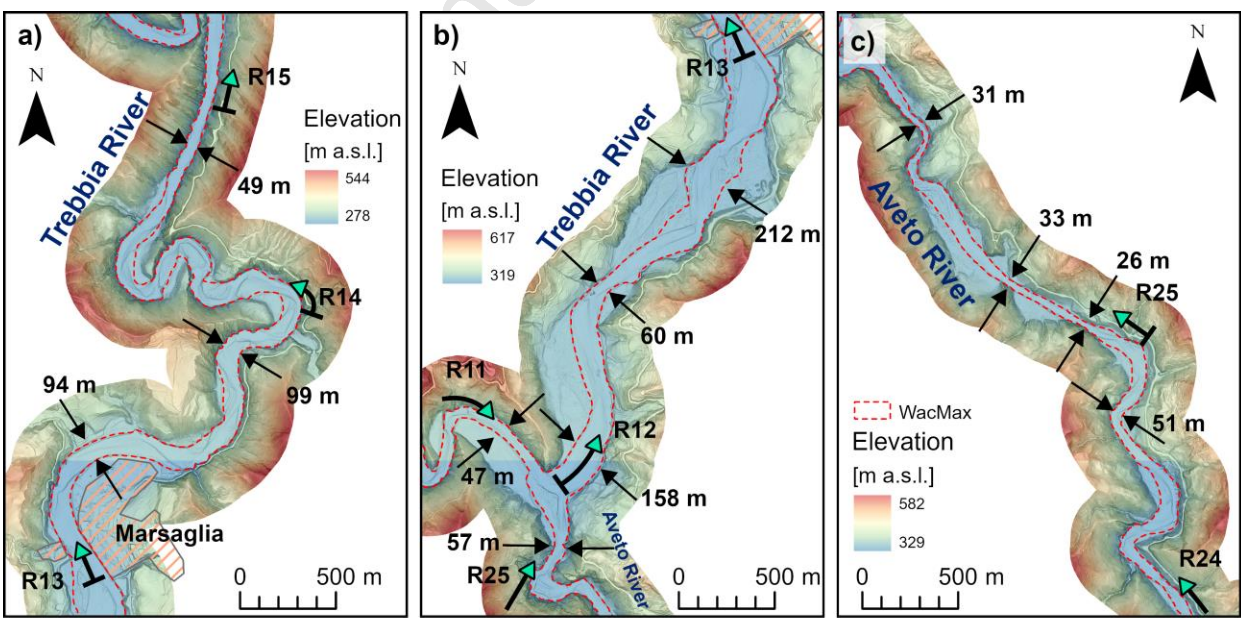


*Figure 13. Detailed 1 m × 1 m LiDAR-derived elevation maps of TAR system sections. The maximum active channel width (WacMax) observed during the 2015 events is delineated by a red dashed line with black arrows indicating representative width measurements at specific locations. a) Lower Trebbia River, downstream of Marsaglia,*

*showing reaches 13, 14, the upper portion of reach 15, and the valley constriction that limits DFSP transport downstream. b) Trebbia-Aveto confluence area, showing the terminal sections of reaches 25 and 11, reach 12, and the upper portion of reach 13, illustrating the valley widening associated with large DFSP storage in reach 12. c) Reaches 24 and 25 of the Aveto River, illustrating the localized valley constrictions within reach 25 that are not captured by the reach-averaged WacMAX.*

### *4.3 Temporal evolution of DFSP storage*

Evaluating the DFSP storage at each timestep reveals three characteristic temporal behaviors among reaches: (i) sustained increase (reaches 3, 6, 9,11,12,13, 17, 21, and 23); (ii) sustained decrease (reaches 2, 5, 10, 14, 15, 19, and 20); or (iii) a peak followed by decline within the study period (reaches 4, 7, 16, 22, 24, and 25) (Figure 14, 15 and 16). Further discussion of DFSP storage evolution for each of the three sections of the TAR system (Upper Trebbia, Aveto, and lower Trebbia) is provided in the following sections.

#### *4.3.1 Upper Trebbia section (Reaches 2–11)*

Overall, the upper Trebbia contains four reaches that show sustained depletion of DFSP storage (reaches 2, 5, 8, and 10), followed immediately downstream by an equal number of reaches that show sustained increase in DFSP storage (reaches 3, 6, 9, and 11), with reaches 4, 7, and 8 representing special cases (Figure 14). Reach 4, which holds the largest DFSP storage in the upper Trebbia, exhibits a sharp increase in storage reaching a peak of ~15% of total DFSP within a few months of the 2015 DF events; thereafter, storage declines slowly but consistently until the end of the study period. Reach 7 also presents a peak, though broad in character, driven by successive intense rainfall events that produce a gradual overall increase in DFSP storage. However, following the most recent intense rainfall in 2021, storage began a gradual decline that became more pronounced after the 2024 rainfall events. Reach 8 presents a contrasting but related pattern: in general, it shows sustained depletion of DFSP storage: however, following the intense rainfall events of 2021, storage begins a slight tendency toward recovery, a trend that becomes more pronounced after the 2024 rainfall events.

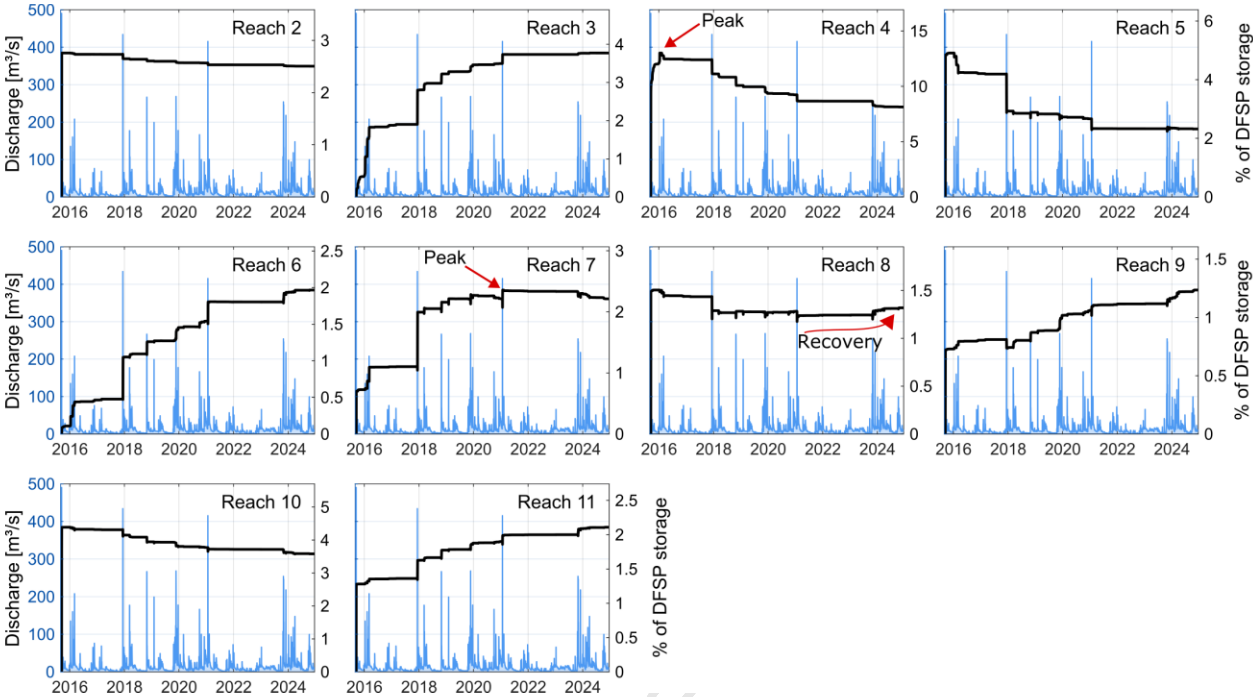


*Figure 14. Temporal evolution of the DFSP storage in the Upper Trebbia reaches during the study period (2015 to 2024).*

### *4.3.2 Aveto section (Reaches 19 –25)*

This area is the most affected by the 2015 DF events. As discussed in Section 4.2, reaches 19–20, despite receiving a substantial volume of DFSP, export most of it downstream due to the high riverbed slopes that promote sediment transport (Figure 15). The DFSP storage of reach19 is completely depleted within a couple of years while reach 20 shows consistent decrease in its storage. The DFSP storage of reach 19 is fully depleted within approximately two years, while reach 20 shows a consistent decrease in storage throughout the study period. In contrast, reach 21, which receives a relatively small DFSP input (Table 1), begins the study period with negligible storage but rapidly accumulates DFSP fed by material remobilized from upstream reaches 19 and 20. Continuing downstream, reach 22 shows a broad peak around 2019, followed by a slow decline in DFSP storage. Reach 24 follows a similar temporal evolution to reach 4 —

coincidentally, both are the reaches with the largest DFSP storage in their respective sections. Reach 24 shows a sharp peak of ~20% of total DFSP, followed by a slow but consistent depletion of its storage. Reach 25, similarly to reach 22, shows a broad peak that occurred later in the study period. The peak of reach 25 appears to be triggered by the 2021 rainfall events, consistent with the behavior observed in reach 7.

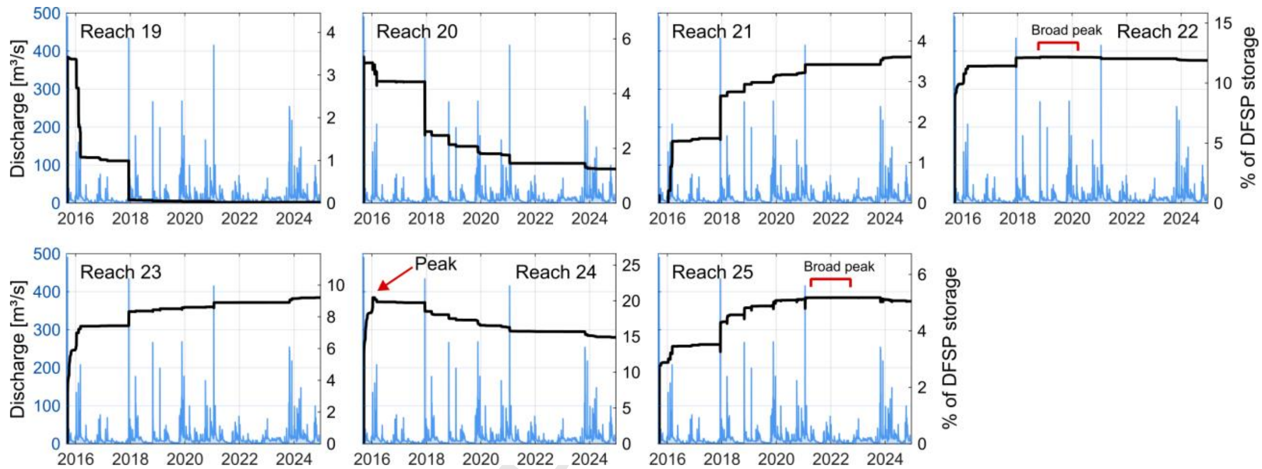


*Figure 15. Temporal evolution of DFSP storage in the Aveto section reaches during the study period (2015 to 2024).*

### *4.3.3 Lower Trebbia section (Reach 12 –17)*

Downstream of the confluence of Trebbia and Aveto Rivers, reaches 12 and 13 show large DFSP storage with a steady increase over time, while reaches 14 and 15 store relatively small volumes, with reach 15 depleting its DFSP storage following the rainfall events of winter 2019–2020 (Figure 16). This steady increase in DFSP storage in reaches 12 and 13 reflects the morphological control on DFSP transport discussed in Section 4.2, which limits further DFSP transport to downstream reaches. Reach 16 shows a peak in DFSP storage by the late 2017, possibly reflecting the deposition of the small fraction of DFSP able to bypass reach 15. This transported material is likely composed predominantly of relatively fine sediment, resulting from hydraulic sorting of bedload due to the differential transport capacity of varying grain sizes. Such fine material is readily transported during moderate flood events after 2018. The negligible DFSP storage in reach 17 is a direct consequence of the retention of most DFSP in upstream reaches.

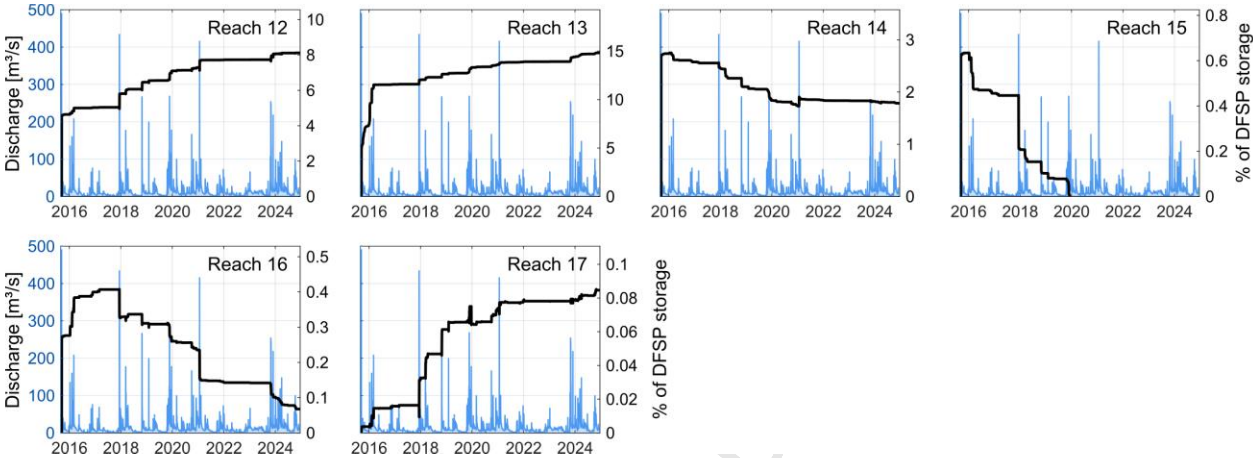


*Figure 16. Temporal evolution of DFSP storage in the lower Trebbia reaches during the study period (2015 to 2024).*

The occurrence of peaks throughout the TAR system suggests that DFSP is continuously being transported and deposited along the main channel. The temporal offset between peaks may indicate that DFSP mobility is expressed as a series of discrete bedload pulses, possibly reflecting the combined influence of hydrogeomorphological controls on bedload transport and hydraulic sorting. Reaches that show a continuous increase in DFSP storage may eventually reach a maximum expressed as a broad peak, before entering a phase of gradual depletion — suggesting a long-term bedload pulse that may reach the basin outlet over timescales exceeding those of the present study.

## 5 Discussion

### *5.1 DFSP export results*

Across all transport formulations in D-CASCADE, our network-scale simulations show that only a small fraction of the DFSP was exported at the basin outlet (generally < 1% with ~10% as the highest), implying that in-basin storage dominates over decadal timescales. This pattern is consistent with previous research: landslide/debris-flow pulses commonly accumulate in headwater and mid-order channels and near tributary junctions and are released intermittently through subsequent events—often over centuries rather than years (Benda and Dunne, 1997; Korup et al., 2004; Lancaster and Casebeer, 2007). Likewise, studies of bed-material waves show that coarse inputs tend to disperse and attenuate rather than translate long distances, constraining downstream delivery and outlet export (Lisle et al., 2000). Sediment-connectivity frameworks for mountain basins highlight how structural barriers (e.g., knickpoints, confinement, and confluences) create bottlenecks and sinks that limit through-routing (Bracken et al., 2015) from DFSP source zones—controls whose influence is suggested by the spatial patterns of DFSP storage identified across the TAR network.

### *5.2 Armoring, active-layer assumptions, and implications for decadal transport*

In mountainous gravel-bed rivers such as the Trebbia River, the bed commonly develops a persistent armored surface that limits sustained transport of finer sediment even during energetic flows (Wilcock and DeTemple, 2005; Ferdowsi et al., 2017). Armor break-up requires high-magnitude floods; otherwise, the protective surface persists and constrains bedload mobility (Houbrechts et al., 2012). D-CASCADE does not explicitly model armoring, instead, it routes sediment through the active-layer concept based on grains-size distribution and flow transport capacity (Tangi et al., 2022). While effective during extreme events that partially break armor, this formulation may lose precision as armoring reforms over years to decades.

Given the magnitude of the September 2015 event, flows likely exceeded thresholds for partial armor break-up, promoting mixing of riverbed material with DFSP inputs. Subsequent re-armoring would tend to bury portions of DFSP beneath the new coarse surface, limiting transport during later, less intense floods (Wilcock and DeTemple, 2005; Mao, 2012; Ferdowsi et al., 2017).

An additional source of uncertainty concerns the GSD sampling strategy. Photo-sieving of bar surfaces may under-represent coarse fractions at the riverbed, potentially lowering the reach GSD that drives transport capacity. Spatial variability in surface GSD due to local bedforms and sediment-supply controls represents a known source of error when sampling is restricted to bars (Billi, 1994; Venditti et al., 2017).

Together, these factors suggest that long-term DFSP transport may be overestimated if re-armoring, burial, and patch-scale heterogeneity are not fully represented in the model, reinforcing the interpretation that basin-scale DFSP export is limited and that storage hotspots dominate the decadal sediment budget.

### *5.3 Grain-size recognition biases*

As noted in Section 3.2.5, the optical resolution of the orthophotos (~2.5–3.0 mm $px^{-1}$) sets a practical detection threshold near 5–6 mm, meaning sand, silt, and clay fractions are not directly resolved. They must be estimated by D-CASCADE, introducing additional uncertainty in transport capacity and routing. However, in steep armored channels, fine fractions supplied during extreme events tend to be efficiently through-routed downstream as traveling bedload over an immobile coarse surface (Schuech et al., 2006; Piton and Recking, 2017); consequently, underestimating sand in the GSD may be less critical for decadal outlet budgets. Conversely, the Wilcock-Crowe transport function explicitly accounts for sand content in gravel mobility. If sand is under-represented in the input GSD, transport capacity may be systematically biased in sandinfluenced reaches. Post-peak hydrograph studies further suggest that fines dominate the immediate export signal while coarse fractions remain stored (Mao, 2012), partially offsetting the impact of fine-fraction underestimation on decadal storage estimates.

For the coarse end of the distribution, pyDGS inputs were capped between 500 and 800 mm to respect D-CASCADE's maximum grain class of ~724 mm ($\varphi \approx -9.5$). Post-2015 orthophotos indicate that large clasts remained largely immobile over the study period, consistent with coarse-patch persistence in armored gravel beds, suggesting that exclusion of the coarsest fraction has limited impact on transport estimates. Finally, pyDGS performance degrades under bimodality, sub-pixel grain conditions, or non-ideal imaging geometry, introducing systematic uncertainty that should be considered when interpreting transport diagnostics derived from image-based GSD (Buscombe, 2013; Buscombe, 2015).

### *5.4 Rainfall distribution and hydrographs*

The rainstorm that triggered the 2015 debris flows occurred in a localized sector of the Trebbia Basin and was characterized by high intensity over a narrow time window (Ciccarese et al., 2020). The basin's hydrological response was accordingly flashy, with sharp rises and short-lived peaks. In D-CASCADE, we employed a daily time step, so discharges were provided as daily mean values. On the event day, the outlet discharge averaged 546.99 $m^3 s^{-1}$ (daily mean), whereas the hourly peak reached approximately 3,000 $m^3 s^{-1}$ for a few hours.

This temporal aggregation smooths hydrograph peaks and can underrepresent brief exceedances of entrainment thresholds, particularly for coarse fractions. Short-duration, high-magnitude flows can mobilize larger clasts and greater volumes of medium gravel that would not be entrained under daily-mean conditions. While at decadal scales this difference may dampen in terms of cumulative export, it can set distinct initial conditions for post-event evolution (e.g., the thickness and sorting of the active layer, spatial patterns of deposition), which in turn may affect long-term trajectories in the model domain.

In this study, we treat the event as a pulse-driven disturbance: the daily time step is appropriate for inter-event storage and routing, but it likely underestimates the initial peak-driven mobilization. Future work could bracket this uncertainty  applying an effective-discharge or peak-over-threshold weighting to better capture the contribution of brief peaks to bedload.

## 6 Conclusion

We assessed the dynamics of the debris-flow sediment pulse (DFSP) in the Trebbia-Aveto River network using a scenario-based comparison — with and without debris-flow sediment pulses — both implemented in D-CASCADE. Five sediment transport equations were tested, and after nearly a decade of simulation, all but one showed that less than 1% of the DFSP was exported from the study area, with only the Parker-Klingeman equation approaching ~10%. These results indicate that in-basin storage dominates over decadal timescales.

Spatially, DFSP storage is concentrated in three settings: immediately downstream of debris-flow source zones in the Trebbia and Aveto rivers, at locations where riverbed slope decreases, and downstream of the Trebbia-Aveto confluence, forming persistent storage hotspots. The temporal analysis revealed reaches where DFSP storage monotonically increased or decreased over the study period, while other reaches exhibited distinct peaks within the decade. These patterns are consistent with slow, pulse-driven downstream transport and intermittent remobilization of DFSP.

Several simplifications were required to apply D-CASCADE successfully, and are theoretically defensible within the geomorphic context of the TAR system. Among the most significant sources of uncertainty are: the expert-based DFSP volume estimate, which relies on a uniform deposit thickness that could not be field-verified across all events; the daily timestep, which smooths hydrograph peaks and likely underestimates initial peak-driven mobilization during the 2015 event; and the reach-averaged active channel width, which conceals localized valley constrictions that act as transport bottlenecks. Additional uncertainties inherent to this type of modeling exercise — including GSD sampling bias, armoring dynamics, and tributary coupling — are acknowledged but considered secondary given the exploratory nature of the analysis.

Looking ahead, model performance could be improved primarily by adopting a finer, hydromorphologically based river network segmentation that better captures localized valley constrictions and their effect on sediment transport; by incorporating sediment inputs from tributaries, hillslopes, and other external sources (e.g., landslides) where structural or functional connectivity is demonstrated; and by refining surface GSD sampling beyond bar surfaces to capture patch-scale heterogeneity. Secondary improvements, including sub-daily hydrological inputs during peak conditions and sensitivity analyses for active-layer thickness and re-armoring dynamics, would further strengthen inference on DFSP storage hotspots. Together, these advances would enhance the transferability of this methodology to other mountain basins where debris-flow pulses shape the decadal sediment budget.



## 7 Acknowledgements

This research has been funded by the Italian Ministry of University and Research, PRIN 2022 Project: “LASST: evaluating LAndslide Sediment Supply to sTreams and connectivity for sustainable, basin-wide sediment management” (cup. B53D23006810006, Associated Investigator: A. Corsini).

## 8 References

Ackers, P. and White, W. R., (1973). Sediment transport: new approach and analysis. Journal of the Hydraulics Division, 99(11),2041–2060. https://doi.org/10.1061/JYCEAJ.0003791

Agisoft, LLC, 2022. Agisoft Metashape Professional (version 1.8.4). https://www.agisoft.com (accessed 16 October 2025).

Arcement, G.J., Schneider, V.R., 1989. Guide for selecting Manning’s roughness coefficients for natural channels and flood plains. U.S. Geological Survey Water-Supply Paper 2339. https://doi.org/10.3133/wsp2339

Benda, L., Dunne, T., 1997. Stochastic forcing of sediment supply to channel networks from landsliding and debris flow. Water Resources Research. 33, 2849–2863. https://doi.org/10.1029/97WR02388

Bennett, G.L., Molnar, P., McArdell, B.W., Schlunegger, F., Burlando, P., 2013. Patterns and controls of sediment production, transfer and yield in the Illgraben. Geomorphology 188, 68–82. https://doi.org/10.1016/j.geomorph.2012.11.029

Billi, P., 1994. Streambed dynamics and grain-size characteristics of two gravel rivers of the Northern Apennines, Italy. In: Ergenzinger, P., Schmidt, K.-H. (Eds.), Dynamics and Geomorphology of Mountain Rivers. Lecture Notes in Earth Sciences, vol. 52. Springer, Berlin, Heidelberg, pp. 197–212. https://doi.org/10.1007/BFb0117840

Bizzi, S., Tangi, M., Schmitt, R.J.P., Pitlick, J., Piégay, H., Castelletti, A.F., 2021. Sediment transport at the network scale and its link to channel morphology in the braided Vjosa River system. Earth Surface Processes and Landforms 46, 2946–2962. https://doi.org/10.1002/esp.5225

Bollati, I.M., Pellegrini, L., Rinaldi, M., Duci, G., Pelfini, M., 2014. Reach-scale morphological adjustments and stages of channel evolution: The case of the Trebbia River (northern Italy). Geomorphology 221, 176–186. https://doi.org/10.1016/j.geomorph.2014.06.007

Bracken, L.J., Turnbull, L., Wainwright, J., Bogaart, P., 2015. Sediment connectivity: A framework for understanding sediment transfer at multiple scales. Earth Surface Processes and Landforms 40, 177–188. https://doi.org/10.1002/esp.3635

Brierley, G.J., Tunnicliffe, J., Bizzi, S., Lee, F., Perry, G., Pöppl, R., Fryirs, K.A., 2022. Quantifying sediment (dis)connectivity in the modeling of river systems. In: Shroder, J.F. (Ed.), Treatise on Geomorphology (2nd ed.). Elsevier, pp. 206–224. https://doi.org/10.1016/B978-0-12-818234-5.00161-9

Bui, V. H., Bui, M. D., and Rutschmann, P., 2019. Advanced numerical modeling of sediment transport in gravel-bed rivers. Water 11(3), 550. https://doi.org/10.3390/w11030550

Buscombe, D., 2013. Transferable wavelet method for grain-size distribution from images of sediment surfaces and thin sections, and other natural granular patterns. Sedimentology 60, 1709–1732. https://doi.org/10.1111/sed.12049

Buscombe, D., 2015. pyDGS—Wavelet-based digital grain size analysis. GitHub. Available at: https://github.com/dbuscombe-usgs/pyDGS (accessed October 2025).

Church, M., Haschenburger, J., 2017. What is the “active layer”? Water Resources Research 53, 5–10. https://doi.org/10.1002/2016WR019675

Church, M., Zimmermann, A., 2007. Form and stability of step-pool channels: Research progress. Water Resources Research 43, W03415. https://doi.org/10.1029/2006WR005037

Ciccarese, G. 2017. Study Of Debris Flow in Emilia Romagna Apennines: rainfall triggering thresholds and hazard analysis at regional scale (PhD dissertation) University of Modena and Reggio Emilia, Modena, Italy. https://morethesis.unimore.it/theses/available/etd-10302017-182507/ (accessed 15.01.2026)

Ciccarese, G., Corsini, A., Pizziolo, M., Truffelli, G., 2016. Debris flows in Val Nure and Val Trebbia (N Apennines) during the September 2015 alluvial event in Piacenza Province (Italy). Rendiconti Online della Società Geologica Italiana 41, 127–130. https://doi.org/10.3301/ROL.2016.110

Ciccarese, G., Mulas, M., Alberoni, P.P., Truffelli, G., Corsini, A., 2020. Debris-flow rainfall thresholds in the Apennines of Emilia-Romagna (Italy) derived by the analysis of recent severe rainstorms and regional meteorological data. Geomorphology 358, 107097. https://doi.org/10.1016/j.geomorph.2020.107097

Ciccarese, G., Mulas, M., Corsini, A., 2021. Combining spatial modelling and regionalization of rainfall thresholds for debris-flow hazard mapping in the Emilia-Romagna Apennines (Italy). Landslides 18, 3513–3529. https://doi.org/10.1007/s10346-021-01739-w

Conti, P., Cornamusini, G., Carmignani, L., 2020. An outline of the geology of the Northern Apennines (Italy), with geological map at 1:250,000 scale. Italian Journal of Geosciences, Vol. 139, No. 2, pp. 149-194. https://doi.org/10.3301/IJG.2019.25

Cordier, F., Tassi, P., Claude, N., Van Bang, D.P., Crosato, A., Rodrigues, S., 2016. Numerical modelling of graded sediment transport based on the experiments of Wilcock and Crowe (2003). In: Bourban, S. (Ed.), Proceedings of the XXIIIrd TELEMAC-MASCARET User Conference 2016, 11–13 October 2016, Paris, France. HR Wallingford, Oxfordshire, pp. 75–83.

Corsini, A., Ciccarese, G., Truffelli, G., 2019. Unusual becoming usual: Recent persistent-rainstorm events and their implications for debris-flow risk management in the northern Apennines of Italy. In: Uljarević, M., Zekan, S., Ibrahimović, Dž. (Eds.), Proceedings of the 4th Regional Symposium on Landslides in the Adriatic Balkan Region, 23–25 October 2019, Sarajevo, Bosnia and Herzegovina. Geotechnical Society of Bosnia and Herzegovina, pp. 13–18.

Cui, Y., 2007. The Unified Gravel-Sand (TUGS) model: Simulating sediment transport and gravel/sand grain-size distributions in gravel-bedded rivers. Water Resources Research 43, W10436. https://doi.org/10.1029/2006WR005330

de Linares, M., Belleudy, P., 2007. Critical shear stress of bimodal sediment in sand–gravel rivers. Journal of Hydraulic Engineering 133, 555–559. https://doi.org/10.1061/(ASCE)0733-9429(2007)133:5(555)

Dhont, B., Ancey, C., 2018. Are bedload transport pulses in gravel-bed rivers created by bar migration or sediment waves? Geophysical Research Letters 45, 5501–5508. https://doi.org/10.1029/2018GL077792

DJI, 2022. DJI Mini 3 Pro—User manual. DJI Technology Co., Ltd. Available at: https://www.dji.com/mini-3-pro (accessed 16 October 2025).

Doolaeghe, D., Bozzolan, E., Argentin, A.-L., Shrestha, S., Pitscheider, F., Capito, L., Cecchetto, M., Brenna, A., Surian, N., Bizzi, S., 2025. Capability of the network scale D-CASCADE model in simulating sediment transport dynamics in various riverine contexts. EGU General Assembly 2025, Vienna, Austria, 27 Apr–2 May 2025, EGU25-17155. https://doi.org/10.5194/egusphere-egu25-17155

Engelund, F., Hansen, E., 1967. A monograph on sediment transport in alluvial streams. Technical University of Denmark 0stervoldgade 10, Copenhagen K. https://resolver.tudelft.nl/uuid:81101b08-04b5-4082-9121-861949c336c9

Ferdowsi, B., Ortiz, C.P., Houssais, M., Jerolmack, D.J., 2017. River-bed armouring as a granular segregation phenomenon. Nature Communications 8, 1363. https://doi.org/10.1038/s41467-017-01681-3

Fryirs, K., 2012. (Dis)connectivity in catchment sediment cascades: A fresh look at the sediment delivery problem. Earth Surface Processes and Landforms 38, 30–46. https://doi.org/10.1002/esp.3242

Gaeuman, D., Andrews, E.D., Krause, A., Smith, W., 2009. Predicting fractional bedload transport rates: Application of the Wilcock–Crowe equations to a regulated gravel-bed river. Water Resources Research 45, W06409. https://doi.org/10.1029/2008WR007320

Heckmann, T., Schwanghart, W., 2013. Geomorphic coupling and sediment connectivity in an alpine catchment—Exploring sediment cascades using graph theory. Geomorphology 182, 89–103. https://doi.org/10.1016/j.geomorph.2012.10.033

Houbrechts, G., Van Campenhout, J., Levecq, Y., Hallot, E., Peeters, A., Petit, F., 2012. Comparison of methods for quantifying active-layer dynamics and bedload discharge in armoured gravel-bed rivers. Earth Surface Processes and Landforms 37, 1501–1517. https://doi.org/10.1002/esp.3258

Hungr, O., Evans, S.G., Bovis, M.J., Hutchinson, J.N., 2001. A review of the classification of landslides of the flow type. Environmental and Engineering Geoscience 7 (3), 221–238.

Jaboyedoff, M., Carrea, D., Derron, M.-H., Oppikofer, T., Penna, I.M., Rudaz, B., 2020. A review of methods used to estimate initial landslide failure surface depths and volumes. Engineering Geology 267, 105478. https://doi.org/10.1016/j.enggeo.2020.105478

Jakob, M., Hungr, O., 2005. Debris-flow hazards and related phenomena. Springer, Berlin, New York, 739.

Jones, K.L., Keith, M.K., Harden, T.M., White, J.S., van de Wetering, S., Dunham, J.B., 2025. Assessment of channel morphology, hydraulics, and bedload transport along the Siletz River, western Oregon. U.S. Geological Survey Scientific Investigations Report 2025–5063, 95 pp. https://doi.org/10.3133/sir20255063

Korup, O., McSaveney, M.J., Davies, T.R.H., 2004. Sediment generation and delivery from large historic landslides in the Southern Alps, New Zealand. Geomorphology 61, 189–207. https://doi.org/10.1016/j.geomorph.2004.01.001

Korup, O., Densmore, A.L., Schlunegger, F., 2010. The role of landslides in mountain range evolution. Geomorphology 120, 77–90. https://doi.org/10.1016/j.geomorph.2009.09.017

Krumbein, W.C., Sloss, L.L., 1963. Stratigraphy and sedimentation. Freeman, San Francisco.

Lancaster, S.T., Casebeer, L.J., 2007. Sediment storage and evacuation in headwater valleys at the transition between debris-flow and fluvial processes. Geology 35, 1027–1030. https://doi.org/10.1130/G239365A.1

Lisle, T.E., Nelson, J.M., Pitlick, J., Madej, M.A., Barkett, B.L., 2000. Variability of bed mobility in natural, gravel-bed channels and adjustments to sediment load at local and reach scales. Water Resources Research 36, 3743–3755. https://doi.org/10.1029/2000WR900238

Mao, L., 2012. The effect of hydrographs on bedload transport and bed sediment spatial arrangement. Journal of Geophysical Research: Earth Surface 117, F03024. https://doi.org/10.1029/2012JF002428

Montgomery, D.R., Buffington, J.M., 1997. Channel-reach morphology in mountain drainage basins. GSA Bulletin 109, 596–611. https://doi.org/10.1130/0016-7606(1997)109<0596:CRMIMD>2.3.CO;2

Monsalve, A., Segura, C., Christiansen, T., and Mullen, A. (2020). A bed load transport equation based on the spatial distribution of shear stress. Earth Surface Dynamics 8, 825–839. https://doi.org/10.5194/esurf-8-825-2020

Nelson, P.A., Morgan, J.A., 2018. Flume experiments on flow and sediment supply controls on gravel bedform dynamics. Geomorphology 309, 239–252. https://doi.org/10.1016/j.geomorph.2018.09.004

Parker, G.,Klingeman, P. C., 1982. On why gravel bed streams are paved. Water Resources Research 18(5),1409–1423. https://doi.org/10.1029/WR018i005p01409

Piton, G., Recking, A., 2017. The concept of travelling bedload and its consequences for bedload computation in mountain streams. Earth Surface Processes and Landforms 42, 1505–1519. https://doi.org/10.1002/esp.4105

Rinaldi, M., Surian, N., Comiti, F., Bussettini, M., 2012. Guidebook for the evaluation of stream morphological conditions by the Morphological Quality Index (MQI), version 1.1. Istituto Superiore per la Protezione e la Ricerca Ambientale (ISPRA), Rome, 85 pp. ISBN 978-88-448-0487-9.

Rinaldi, M., Surian, N., Comiti, F., Bussettini, M., 2013. A method for the assessment and analysis of the hydromorphological condition of Italian streams: The Morphological Quality Index (MQI). Geomorphology 180–181, 96–108. https://doi.org/10.1016/j.geomorph.2012.09.009

Schlunegger, F., Badoux, A., McArdell, B.W., Gwerder, C., Schnydrig, D., Rieke-Zapp, D., Molnar, P., 2009. Limits of sediment transfer in an alpine debris-flow catchment, Illgraben, Switzerland. Quaternary Science Reviews 28, 1097–1105. https://doi.org/10.1016/j.quascirev.2008.10.025

Schmitt, R.J.P., Bizzi, S., Castelletti, A., 2016. Tracking multiple sediment cascades at the river network scale identifies controls and emerging patterns of sediment connectivity. Water Resources Research 52, 3941–3965. https://doi.org/10.1002/2015WR018097

Schmitt, R.J.P., Bizzi, S., Castelletti, A., Kondolf, G.M., 2018. Improved trade-offs of hydropower and sand connectivity by strategic dam planning in the Mekong. Nature Sustainability 1, 96–104. https://doi.org/10.1038/s41893-018-0022-3

Schuerch, P., Densmore, A.L., McArdell, B.W., Molnar, P., 2006. The influence of landsliding on sediment supply and channel change in a steep mountain catchment. Geomorphology 78, 222–235. https://doi.org/10.1016/j.geomorph.2006.01.025

Schwanghart, W., Scherler, D., 2014. TopoToolbox 2 – MATLAB-based software for topographic analysis and modeling in Earth surface sciences. Earth Surface Dynamics

2, 1–7. https://doi.org/10.5194/esurf-2-1-2014

Scorpio, V., Crema, S., Marra, F., Righini, M., Ciccarese, G., Borga, M., Cavalli, M., Corsini, A., Marchi, L., Surian, N., Comiti, F., 2018. Basin-scale analysis of the geomorphic effectiveness of flash floods: A study in the northern Apennines (Italy). Science of the Total Environment 640–641, 337–351. https://doi.org/10.1016/j.scitotenv.2018.05.252

Shih, S.-M., Komar, P. D. (1990). Differential bedload transport rates in a gravel-bed stream: A grain-size distribution approach. Earth Surface Processes and Landforms 15(6):539–552. https://doi.org/10.1002/esp.3290150606

Tangi, M., Schmitt, R.J.P., Bizzi, S., Castelletti, A., 2019. The CASCADE toolbox for analyzing river sediment connectivity and management. Environmental Modelling and Software 119, 400–406. https://doi.org/10.1016/j.envsoft.2019.07.008

Tangi, M., Bizzi, S., Fryirs, K., Castelletti, A., 2022. A dynamic, network-scale sediment (dis)connectivity model to reconstruct historical sediment transfer and river reach sediment budgets. Water Resources Research 58, e2021WR030784. https://doi.org/10.1029/2021WR030784

Tangi, M., Bizzi, S., Schmitt, R.J.P., Castelletti, A., 2023. Balancing sediment connectivity and energy production via optimized reservoir sediment management strategies. Water Resources Research 59, e2022WR034033. https://doi.org/10.1029/2022WR034033

Uchida, T., Sakurai, W., Iuchi, T., Izumiyama, H., Borgatti, L., Marcato, G., Pasuto, A., 2018. Effects of episodic sediment supply on bedload transport rate in mountain rivers: Detecting debris-flow activity using continuous monitoring. Geomorphology 306, 198–209. https://doi.org/10.1016/j.geomorph.2017.12.040

Vazquez-Tarrío, D., Menendez-Duarte, R., 2015. Assessment of bedload equations using data obtained with tracers in two coarse-bed mountain streams (Narcea River basin, NW Spain). Geomorphology 238, 78–93. https://doi.org/10.1016/j.geomorph.2015.02.032

Venditti, J.G., Nelson, P.A., Bradley, R.W., Haught, D., Gitto, A.B., 2017. Bedforms, structures, patches, and sediment supply in gravel-bed rivers. In: Tsutsumi, D., Laronne, J.B. (Eds.), Gravel-Bed Rivers: Processes and Disasters. John Wiley and Sons Ltd., pp. 439–466. https://doi.org/10.1002/9781118971437.ch16

Wilcock, P. R. (2001). Toward a practical method for estimating sediment-transport rates in gravel-bed rivers. Earth Surface Processes and Landforms 26(13), 1395–1408. https://doi.org/10.1002/esp.301

Wilcock, P.R., Crowe, J.C., 2003. Surface-based transport model for mixed-size sediments. Journal of Hydraulic Engineering 129, 120–128. https://doi.org/10.1061/(ASCE)0733-9429(2003)129:2(120)

Wilcock, P.R., DeTemple, B.T., 2005. Persistence of armor layers in gravel-bed streams. Geophysical Research Letters 32, L08402. https://doi.org/10.1029/2004GL021772

Wong, M. and Parker, G., 2006. Reanalysis and correction of bed-load relation of Meyer-Peter and Müller using their own database. Journal of Hydraulic Engineering 132(11),1159–1168. https://doi.org/10.1061/(ASCE)0733-9429(2006)132:11(1159)

Wu, B., Molinas, A., and Shu, A. (2003). Fractional transport of sediment mixtures. International Journal of Sediment Research 18(3),232–247.

Yang, C. T., 1973. Incipient motion and sediment transport. Journal of the Hydraulics Division, ASCE 99(HY10), 1679–1704.

Yang, C. T., 1984. Unit stream power equation for gravel. Journal of Hydraulic Engineering 110(12):1783–1797. https://doi.org/10.1061/(ASCE)0733-9429(1984)110:12(1783)

**Abstract**

Debris flows can dominate sediment budgets in mountain basins, yet their basin-scale routing, residence times, and outlet export remain difficult to quantify. We analyze the Trebbia-Aveto River (TAR) network in northern Italy following the September 2015 event, which produced localized, high-intensity rainfall and multiple debris flows. Using D-CASCADE, a dynamic sediment (dis)connectivity model, we compare two scenarios — with and without debris-flow inputs — to quantify the downstream routing, storage, and basin-scale export of the debris-flow sediment pulse (DFSP) through the TAR river network over nearly a decade. Simulations with five sediment transport equations indicate that less than 1% of the DFSP was exported at the basin outlet in most cases, with in-basin storage dominating over a decadal timescale. Storage hotspots concentrate downstream of debris-flow source zones in the Trebbia and Aveto rivers, at locations of riverbed slope reduction, and downstream of their confluence. Reach-scale time series reveal three characteristic behaviors — monotonic increase, monotonic decrease, and pulse-driven peaks within the study period — consistent with slow, intermittent DFSP remobilization driven by successive rainfall events. Although results are subject to uncertainties inherent to model-based approaches, the spatial and temporal patterns of DFSP storage are broadly consistent with theoretical understanding of sediment dynamics in armored gravel-bed mountain rivers. This work demonstrates that network-scale sediment connectivity modeling offers a tractable and reproducible framework for reconstructing debris flow-derived sediment dynamics at the basin scale.

**Declaration of interests**

☒ The authors declare that they have no known competing financial interests or personal relationships that could have appeared to influence the work reported in this paper.

☐ The authors declare the following financial interests/personal relationships which may be considered as potential competing interests:

**Highlights**

- D-CASCADE model isolates debris-flow impacts on the Trebbia–Aveto sediment budget.
- Debris-flow pulses dominate decadal storage with only 0.93% exported at the outlet.
- Storage hotspots occur at confluences and reaches below high-density source areas.